

1 **The microstructural evolution of cementitious, flexible**
2 **waterproofing membranes during deformation with special focus**
3 **on the role of crazing**

4 Marius Waldvogel^{1*}, Roger Zurbriggen², Alfons Berger¹, and Marco Herwegh¹

5

6 1 Institute of Geological Sciences, University of Bern, Baltzerstrasse 1+3, 3012 Bern,
7 Switzerland

8 2 Nouryon Chemicals AG, Industriestrasse 17a, 6203 Sempach Station, Switzerland

9 * Corresponding author: marius.waldvogel@geo.unibe.ch

10 **Abstract**

11 The initiation and evolution of deformation-induced (micro)structures in one-component,
12 cementitious, flexible waterproofing membranes is investigated combining normed crack-
13 bridging (EN14891) with image analysis of in-situ photos acquired by optical and scanning
14 electron microscopy. The permanent deformation of the polymer matrix concentrates in a
15 trapezoidal deformation volume and subdivides into an active and a passive part. During the
16 active part, the polymer matrix stretches and fibril-void microstructures (FVM) form. The
17 ubiquitously present heterogeneities (quartz grains, cement particles and air pores) act as
18 stress concentrators. After FVMs reach their maximum density inside the deformation
19 volume, straining by passive stretching until final rupturing takes over. Starting at the
20 substrate-membrane interface, the cracking propagates through the membrane along
21 aforementioned heterogeneities and the spatially distributed FVMs. Linking mechanical
22 behaviour and deformation structures is therefore crucial to (i) understand the complex
23 elasto-plastic deformation and to (ii) develop new products increasing the durability of the
24 protective system.

25 **Keywords**

26 crack-bridging; waterproofing membrane; permanent deformation; (micro)structures

27 **1. Introduction**

28 Cracking of concrete can be induced by several mechanisms [1] and causes severe damage
29 to concrete structures both through the cracking and the subsequent degradation by water
30 ingress [2]. Concrete and other cement-based materials are prone to cracking as they have
31 a low tensile strength only. In the building industry, the tensile strength of cement-based
32 products like mortars is commonly enhanced by polymer modification because pure
33 polymers show a high tensile strength [3,4]. Due to their improved tensile strength and
34 extensibility [3], these polymer-modified mortars (PMMs) prevent the propagation of cracks
35 formed in the substrate (hygrical shrinkage, thermal expansion/contraction etc.) into above
36 laying systems (e.g. tilings) by stretching above the (micro)crack forming in the substrate
37 and stopping its propagation out of the substrate [5–7] (Fig. 1). This behaviour, called crack-
38 bridging ability (CBA), is the reason for the use of PMMs as waterproofing membranes at
39 instances where constructions are in contact with water like bathrooms, swimming pools,
40 roofings or underground facades. Modification can be done by adding the polymer as
41 dispersion or as redispersible polymer powder (RPP) [8–10]. Addition of the polymer takes
42 place directly prior to the production of the fresh slurry. From a logistic [8–11], environmental
43 [8–11] and performance [8,11,12] point of view, the RPP modification is advantageous. In
44 their hardened state, PMMs represent a composite material consisting of brittle fillers. Here
45 quartz grains, hydrated and unhydrated cement particles, and mixing entrained air pores are
46 incorporated in a polymer matrix. Polymer composites subdivide into two groups. The first
47 group covers polymer matrixes containing rubber particles. The matrix is brittle and the
48 incorporated particles are ductile [13]. The second group describes polymer matrixes with
49 incorporated inorganic nanoparticles [13]. In this group, the filler material is more brittle than
50 the polymer matrix. Several studies deal with the deformation behaviour and deformation
51 structures in uniaxial tension for the respective group. For both groups, deformation relates
52 to stress concentrations forming around the particles (rubber or inorganic) inside the polymer
53 matrix [13–18]. Deformation structures found in the first group of polymer composites are
54 crazing in between the rubber particles [13,19,20], void formation [15,21], shear yielding in

55 between rubber particles [13,15,20,22,23] and crack blunting at the rubber particles [24]. The
56 second group deforms by debonding at the nanoparticle-matrix interface [18,19,21], plastic
57 void growth [17,18] and craze-like microstructures [13,25]. Crazing, mentioned as
58 deformation structure in both groups, is a deformation mechanism originally found in
59 amorphous polymers below their glass transition temperature (T_g). It describes local plastic
60 deformation [26–28] which starts as micro- and nano-voids [26–35] developing to an
61 alternating sequence of fibrils and voids [28,30,36] oriented parallel to the extension
62 direction [37] and finally resulting in fibril rupture and therefore, cracking [27,28,31,37–39].
63 Studies dealing with organic coating relate the CBA to the total failure of the organic coating
64 mechanical tests [2,40,41]. Furthermore, combining data of both, dog-bone tests and crack-
65 bridging tests, relate the crack-bridging ability with the mechanical behaviour of those
66 organic coatings [40]. Further investigations show that the failure of the coating starts at the
67 substrate-coating interface and migrates vertically towards the coating's surface [40]. The
68 deformation behaviour in the present cement composites currently lacks a profound
69 understanding. So far crack bridging tests according to norms provide the only information
70 about the crack-bridging ability of waterproofing membranes. Studies dealing with the
71 appearance of white spots and lines on surfaces of waterproofing membranes and relating
72 them to domains of local strain concentrations [42,43] are the only information dealing with
73 deformation-induced structures in waterproofing membranes. Detailed investigations of the
74 active failure processes during crack bridging of a waterproofing membrane are missing. We
75 close this gap by combining crack-bridging experiments with quantitative (micro)-structural
76 analysis in order to detect the involved deformation processes. The latter is exerted on in-
77 situ photographs, optical microscopy and scanning electron microscopy (SEM). Based on all
78 results we suggest a subsequent progression of deformation processes with a link to the
79 bulk mechanical behaviour of the waterproofing membrane during crack-bridging.

80 **2. Methods**

81 This study focusses on liquid-applied, one-component, cementitious, flexible waterproofing
82 membranes. In the used standard formulation, a waterproofing membrane consists of quartz
83 grains (0.1 – 0.3 mm in diameter), Ordinary Portland Cement (OPC, 52.5 N) and an ethylene
84 vinyl-acetate (EVA) based redispersible polymer powder (RPP). The choice of the
85 appropriate amount of RPP is based on several factors: First, the optimum polymer content
86 in crack isolation floor systems is considered to be between 20-35 wt.% [44]. Second, RPP
87 contents >25 wt.% only increase the crack-bridging, while the maximum load and hence
88 stress the membrane can bear remains constant from 25 wt.% RPP onwards [45]. Third,
89 from 25 wt.% onwards, the waterproofing membrane represents the volumetrically dominant
90 phase in the composite material [45]. Therefore, it can be assured that the mechanisms
91 being active during crack bridging are governed by the mechanical behaviour of the RPP. In
92 order to produce samples for crack-bridging tests and dog-bone tests, a slurry is produced
93 by mixing the individual components (dry mix) and adding water in the appropriate amount
94 (see Tab. 1 for weight percentages of individual components). For crack-bridging samples,
95 the freshly mixed slurry is applied on both sides of two juxtaposed fibre cement boards
96 (substrate in this study) and is cured for 28 days at 23°C and 50% relative humidity.
97 Afterwards, the fibreboards are cut by a Con-Star 35/60 saw into 160 mm by 30 mm
98 samples. The application and sample preparation process is described in detail in [46] and
99 summarised in Figure 2. The volumetric composition of the hardened waterproofing
100 membrane is based on point counting of thin-sections and is provided in Table 2. In contrast
101 to the norm defining the geometry and production of crack-bridging samples as well as the
102 crack-bridging test [47], the initial gap is not produced by bending the cured sample in a jig.
103 Instead we simulate the crack by juxtaposing two substrate plates prior to the slurry
104 application. This modification was done in order to avoid bending-induced pre-damage (e.g.
105 debonding of the waterproofing membrane) as this might already influence the results of
106 crack-bridging tests significantly [41]. For dog-bone samples, the freshly mixed slurry is
107 applied as plane membrane on a plastic film and is cured for 28 days at 23°C and 50%
108 relative humidity. Afterwards, individual dog bones are punched-out by a blade. The

109 geometries of the dog bone are defined by type 5 of the according norm [48]. Both, crack-
110 bridging and dog bone tests, are exerted using a Z020/TH2S by Zwick/Roell™ (Fig. 3a).
111 Testing speeds are set to 0.15 mm/min for the crack-bridging samples and 100 mm/min for
112 the dog-bone samples following [47] and [48] respectively For both sample types, nominal
113 stress is calculated by using the individual sample geometry. Furthermore, nominal strain is
114 calculated for dog-bone samples based on their individual geometry. Every experiment is run
115 until a total failure of the sample occurred and recorded with time-lapse photography (Fig.
116 3b). For the crack-bridging samples, the exact point of failure defined in [47] is determined
117 by revisiting the acquired photographic time-lapse sequences. For all crack-bridging
118 samples, the surface evolution of lateral strain localisation is optically traced by detecting
119 strain whitening [42] domains in the time-lapse photographs. This image analysis is exerted
120 using Fiji [49] modified with the Xlib and shape filter [50] plugins. On the processed images
121 (Fig.4 a2-d2), the width of the strain-whitening zone is measured perpendicular to its long
122 axis along lines separated by 1 mm distance. Obtained width values are then averaged. The
123 outermost 5 mm on each side of the sample are discarded, in order to exclude potential
124 edge effects (red shaded areas in Fig. 4a-d) [45]. Additionally, the number of white spots and
125 their respective widths are mapped in every tenth photograph (i.e. steps of 100 μ m
126 displacement) along three lines (green dashed lines in Fig.4 a2-d2) and then averaged. The
127 spacing between the three lines is set large enough to assure that no line was counted twice
128 (green dashed lines in Fig.4 a2-d2). In an additional set of crack-bridging experiments, the
129 respective experiment is stopped at a predefined displacement; the sample is stabilized
130 allowing manufacturing of thin-sections (Fig. 3c, d). Stabilisation is done by gluing plastic
131 wedges into the open substrate gap using a fast-setting, two-component epoxy. Due to their
132 shape, the plastic wedges fit in all open substrate gaps without any pushing. Resulting thin-
133 section series therefore represent snap-shots at given displacements allowing investigating
134 damage evolution in sections parallel to the extension direction but perpendicular to the
135 fibreboard planes (Fig. 3d, Tab. 3). Thin-sections are investigated using optical light
136 microscopy. The surface of a piece of a strained crack-bridging sample is examined using

137 scanning electron microscopy (SEM, Zeiss Evo 50, variable pressure mode, gas pressure in
138 the chamber =21 Pa, beam current = 500pA, acceleration voltage = 11.69 kV). Using the
139 SEM in variable pressure mode allows observations without coating the sample. Additionally,
140 continuous degassing of the large-sized porous, crack-bridging sample counteracts the
141 stability of the high vacuum configuration. However, the spatial resolution is somewhat
142 reduced in the variable pressure mode. In order to circumvent these problems, stretched
143 samples of just the waterproofing membrane (5 mm by 2 mm, no substrate) are coated by
144 gold and studied under high-vacuum SEM conditions (beam current = 250pA, acceleration
145 voltage = 6kV). Note that all optical investigations were performed to image the deformation
146 evolution prior to failure of the waterproofing membrane.

147 **3. Results**

148 **3.1 Crack-bridging samples**

149 **3.1.1 Sample's surface**

150 Using the time-lapse photographs, four important moments during the sample's surface
151 evolution are identified (Fig. 4). (i) *Discontinuous-Strain-Whitening* marks the moment at
152 which a first strain whitening spot occurs on the sample's surface. (ii) *Continuous-Strain-*
153 *Whitening* marks the moment at which a first line of strain whitening spans over the entire
154 sample width. (iii) *First Failure* marks the time at which the waterproofing membrane is not
155 watertight anymore, i.e. the occurrence of a fracture dissecting the entire membrane
156 vertically [47]. (iv) *Final Failure* marks the displacement at a vertical continuous crack spans
157 across the entire width of the waterproofing membrane. This defines the end of the
158 experiment. Close-up pictures show an initially homogeneous surface of the waterproofing
159 membrane with only air pores and quartz grains as heterogeneities (Fig. 5a). From early
160 stages of strain whitening onwards, the whitening domains preferentially bend around quartz
161 grains (orange rectangle in Fig. 5b) and run perpendicular to pore rims (blue rectangle in Fig.
162 5b). Additionally, elliptical holes start to form in polymer matrix. The long axes of the elliptical
163 holes are parallel to the tensile loading direction (red arrows in Fig. 5b). During a late stage

164 of the strain whitening, aligned arrays of elliptical holes appear along strain whitening lines
165 (red rectangle in Fig. 5c). Some of the former individual elliptical holes laterally connect with
166 each other forming a crack with a lobate boundary (red dashed rectangle in red rectangle in
167 Fig. 5c). This connection often starts from pore rims highlighting the role of the pores for
168 crack initiation (pink arrow in Fig.5c). Subsequently, cracks propagate progressively into the
169 membrane by connecting either individual or already connected elliptical holes preserving
170 the lobes in the perimeter (green arrow in Fig. 5d). Time-lapse photography also allows
171 mapping the evolution of the zone in which the strain whitening occurs with increasing
172 opening of the substrate gap. This *Strain Whitening Width* (SWW) starts to evolve (Fig. 6a),
173 i.e. deviate from 0, with the *Discontinuous Strain Whitening* (grey line in Fig. 6). As prior to
174 the *Continuous Strain Whitening* the white spots appear only locally on the membrane's
175 surface, a continuous evolution is possible from the *Continuous Strain Whitening* (pink line in
176 Fig. 6) onwards. From there, the SWW grows linearly with a steep slope (purple shaded area
177 in Fig. 6). The growth rate decreases at a displacement around 950 μm (green shaded area
178 in Fig. 6). This moderate slope is steady until the *Final Failure* (black line in Fig. 6) of the
179 sample. Additionally to the growth behaviour of the zone of strain whitening, the number of
180 strain whitening spots and their respective width change with increasing substrate gap
181 opening and is linked to the slope of the SWW. As long as the slope is steep i.e. from the
182 *Continuous Strain Whitening* onwards, the number of strain whitening spots increases while
183 their respective width is constant (Fig. 6b). This characteristic of the individual strain
184 whitening spots changes with the change in the slope of the SWW evolution. From there
185 onwards, the number of strain whitening spots is constant but they increase in their
186 respective width (Fig. 6c).

187 **3.1.2 Microstructures in 2D along the membrane's thickness (Optical microscopy)**

188 Optical microscopy of thin sections reveals an alternating arrangement of stretched polymer
189 fibrils and elliptical shaped voids in between the individual fibrils (Fig. 7). Both, the fibrils and
190 the long axes of the voids show an orientation subparallel to the direction of the tensile load

191 (Fig. 7). This fibril-void microstructure (FVM) represents straining of the polymer film; and
192 therefore, mapping of film-related deformation structures (FVM and cracks) on photos of
193 thin-sections (Fig. 8a-d) is crucial to understand the film-related deformation structures and
194 evolution. The triple junction between membrane-substrate interface and artificial fibreboard
195 crack represents the starting point for both straining (Fig. 8e) and subsequent cracking (Fig.
196 8f, g). With increasing opening of the substrate crack, both migrate towards the surface of
197 the upper and lower membrane (Fig. 8g and h). FVM initiate and propagate (i) in front of
198 crack tips (Figs. 7, 8f-h) and (ii) randomly at heterogeneities (air pores or quartz grains)
199 inside a corridor of ca 2.5 mm to each side of the position of the substrate crack. Note that
200 this distance coincides excellently with the strain whitening widths measured at the sample's
201 surface (Fig. 6a). Contrarily to the randomness regarding the appearance inside the corridor,
202 the position of the FVM at the respective heterogeneity is systematic and is revealed by
203 observing the thin-sections in detail (red, dashed rectangle in Fig. 8c). The presence of
204 quartz grains deviate the FVM towards the polar region (explained in discussion, see Fig.
205 16) of the respective quartz grain (Fig. 5b orange rectangle, Figs. 8f-h 9b, c black arrows).
206 After approaching the respective quartz grain, the FVM propagates along the quartz grain-
207 polymer matrix interface (Fig. 9b,c black arrows). Contrarily, air pores cause FVM
208 propagation towards the equator (explained in discussion, see Fig. 16) of the respective air
209 pore (Figs. 8f-h, 9d, e). When connecting two air pores, the FVM runs in the straightest
210 possible way in between their respective equatorial region. As a function of increasing
211 fibreboard displacement, the number of spots of strained polymer film increases (Fig. 8e-g)
212 but decreases from the moment on once a continuous crack is present (Fig. 8h). The
213 detailed investigation of the thin sections also shows that the perimeter of the cracks shows
214 straight and convex parts (Fig. 9a).

215 **3.1.3 Microstructures at high resolutions (Scanning Electron Microscopy)**

216 Using scanning electron microscopy (SEM) reveals the deformation structures which form in
217 a strained waterproofing membrane which macroscopically shows strain whitening (Fig.

218 10a). Overview images (Fig. 10a, b), show a rough morphology in non-strained areas. This
219 topography is caused by quartz grains on a large scale (Fig. 10a, b) and by cement grains
220 on a small scale (Fig. 10d, e). The topography significantly flattens in those parts of the
221 waterproofing membrane being affected by strain whitening, i.e. the strained membrane (Fig.
222 10a, b). Present quartz grains govern the path of the strain whitening as the strain whitening
223 bends around the quartz grains (Fig. 10a). The strain whitening evolves gradually from non-
224 strained areas (Fig. 10c) over white (Fig. 10a blue arrow, d, e) to transparent (yellow arrow
225 in Fig. 10a). The white part shows the strained polymer matrix of the waterproofing
226 membrane still containing remnant structures of primary latex particles and cement grains
227 incorporated in the strained matrix (Fig. 10d and e). Non-strained areas also contain
228 remnant structures of primary latex particles (Fig. 10c). In the transparent part, the strained
229 polymer film is smooth and free of cement particles (Fig. 10e). Additionally, the transparency
230 of the membrane indicates a strong thinning of the film. Furthermore, voids initiate and grow
231 inside the high strain zone. Voids initiate and terminate at heterogeneities (here cement
232 grain, Fig. 10e-g). At initiation, voids are in the range of 150-300 nm and roundish (Fig. 10g).
233 Very soon after initiation, their shape changes to elliptical with the long axis being oriented
234 parallel to the tensile load direction (Fig. 10g). Mature voids show large ranges in size and
235 are strongly elliptical with the same orientation of their respective long axis (Fig. 10b, f).
236 Some of the mature voids are vertically continuous (blue dot in Fig. 10f) while others still
237 show an intact polymer film beneath the voids (green dot in Fig. 10f). The mature voids are
238 separated by strained polymer matrix. Based on these observations, we claim that the white
239 part of the strained membrane represents an early deformation stage while the transparent
240 part equals to a late deformation stage. At the rim of the zone representing the late
241 deformation stage, the strained polymer film changes gradually from thin, smooth particle-
242 free and void-containing to a strained polymer film containing latex and cement particles
243 (Figs. 10e, 12). A SEM profile (red dot in Fig. 10a indicates the profile line in planar view)
244 along the thickness of this strained waterproofing membrane reveals the formation of
245 deformation structures in the third dimension. Deformation, expressed in form of an FVM,

246 takes place in vicinity of an air pore (Fig. 11). The FVM occurs in the equatorial region of the
247 air pore relative to the tensile load direction, which is in agreement with the orientation of the
248 FVM relative to air pores in the thin section (Fig. 8g and h). The size of the voids decreases
249 with increasing distance from the pore rim which indicates that the FVM initiated at the pore-
250 membrane interface and propagates into the polymer matrix (Fig. 11b and c). SEM of the
251 surface of a deformed and fixed crack-bridging sample shows similar features (Fig. 12). On
252 this surface, local FVMs oriented parallel to the tensile load direction indicate deformation.
253 First of all, the area around the FVM is brighter than the rest of the waterproofing membrane
254 (white ellipse in Fig. 12a) which indicates a high local straining of the polymer matrix.
255 Second, highly-stretched parts of the polymer matrix in between the voids are smooth are
256 thin, particle-free and show zones of darker colour which appear to be thinner and indented
257 (black arrows in Fig. 12b). These latter features probably represent spots in which new voids
258 will form. Zones of low-strained polymers film contain latex and cement particles and
259 increasingly appear towards the rim of the FVM (white arrows in Fig. 12b). The alternating
260 sequence of mature voids and strained polymer film found on a planar view, combined with
261 the FVM found in the cross-section views in thin-sections and in the SEM profile along the
262 thickness of the strained membrane, indicates that deformation structures in general and the
263 FVM in particular are three-dimensional (Fig. 13).

264 **3.2 Dog bone samples**

265 The stress-strain data, recorded by the tensile rig, define the bulk material's mechanical
266 response in terms of elastic and plastic deformation. As soon as a deviation from linear
267 stress-strain behaviour occurs, the material reaches its elastic yield strength. On average,
268 the dog bone samples yield elastically at 2 % strain and at 2.8 MPa stress (red arrow in Fig.
269 14). Afterwards, the bulk samples exhibits permanent deformation. Further important
270 material parameters are the maximum stress the bulk material can withstand and the strain
271 at which the sample fail. The average maximum stress is 4 MPa and appears at 26% strain
272 (blue arrow in Fig. 14). Sample failure occurs at 29.9% strain (green arrow in Fig. 14) Due to

273 the constant monitoring of the dog bone's surface during the experiment, identification of
274 surface features is possible. Noticeable features occurring on the dog bone surface are the
275 *Discontinuous Strain Whitening* and the *First Failure*. The definition of these two features is
276 the same as for the crack-bridging samples (Fig. 4a, c). The knowledge of the displacement
277 of every recorded image allows the integration of the two observed features into the stress-
278 strain behaviour of the bulk dog bone. The *Discontinuous Strain Whitening* appears after the
279 elastic yield, i.e. the bulk membrane is already in a state of permanent deformation (Fig. 14).
280 The *First Failure*, i.e. the lack of water tightness appears shortly after peak stress (Fig. 14).
281 Post first failure deformation leads to growth of the first crack to complete sample rupture.

282 **4. Discussion**

283 **4.1 Crazeing as deformation mechanism in waterproofing membranes**

284 The evolution of deformation structures in tension is best known and described for
285 amorphous, glassy polymer films. Plastic deformation initiates at heterogeneities (scratches,
286 dust particles, imperfections, artificially induced) by the formation of nanovoids [51,52]. With
287 ongoing deformation, the nanovoids grow resulting in a microstructure of stretched polymer
288 fibrils with intercalated voids [28,30,31,37,39,53]. The diameter of the individual features
289 inside one craze ranges between 5 and 50 nm [54,55]. Both, the fibrils and voids are
290 oriented parallel to the tensile load direction [28,30,31,37,39,53]. This microstructure is
291 known as crazes and its formation process is called crazeing. With further deformation, the
292 fibrils stretch and elongate plastically [31,38,51,53]. The highly strained fibrils grow by
293 drawing in material from the rim surrounding the craze microstructure [51,54]. This rim
294 represents a locally low-strained polymer film. Outside of this structure, the polymer film is
295 under bulk strain conditions. The fibrils rupture when their maximum stretching capacity is
296 reached and from that moment onwards, a crack initiates and follows the craze
297 microstructure [27,28,31,37–39]. The craze microstructure itself propagates perpendicular to
298 the tensile load direction as nanovoids form at the craze tip [30]. Figure 15 summarises this
299 described evolution of the deformation structure. Although well-known from amorphous,

300 glassy polymers, crazing occurs not exclusively in this material but craze-like microstructures
301 form also in amorphous and semi-crystalline polymers above their glass transition
302 temperature (T_g) [54,56,57] and in polymer composites [13]. The FVM observed in our
303 experiments in both light and scanning electron microscopy (i) initiates as microvoids at rigid
304 particles which act as heterogeneities in a pure polymer film (Fig. 8f and g), (ii) develops to
305 fibrils and voids being oriented parallel to the tensile load direction (Figs. 8f,g, 9, 10), (iii)
306 shows internal zonation from a high strained centre to a low strained rim in the deformation
307 structure (Figs. 10e, 12) and (iv) ruptures in a brittle manner by breakdown of the individual
308 fibrils. All these evolutionary steps of the FVM occur in a polymer matrix above its T_g . These
309 observations lead to the claim that, on a micron-level, the plastic deformation in the
310 investigated waterproofing membranes is a craze-like microstructure starting with (i)
311 microvoid formation leading to (ii) FVM initiation and propagation and ending with (iii) brittle
312 fibril rupture, i.e. cracking. However, the size range of the individual fibrils and voids inside
313 the FVMs correlates better with size ranges for fibrils and voids occurring in semi-crystalline
314 polymers than in amorphous polymers [55]. Strain-induced orientation is a known plastic
315 deformation mechanism occurring when stretching originally amorphous polymers at
316 temperatures above their T_g [56,58–61]. Furthermore, the strain-induced orientation can
317 cause macroscopically observable whitening [62]. Hence, the occurrence of strain-induced
318 whitening on the membrane's surface (see 4.3) provides another hint to a strain-induced
319 orientation of the polymer matrix. Therefore, strain-induced orientation may precede
320 microvoid formation and forms the very first plastic deformation structure on a sub-micron
321 level. However, the presence of strain-induced orientation is solely based on indirect
322 observations.

323 **4.2 From incipient strain localisation to sample failure**

324 Crazing requires overcoming a threshold in stress [38,51,63] or strain [64,65], so its
325 formation appears at spots of localised plastic deformation. Hence, the mapped FVM is a
326 proxy to investigate the initiation and propagation of plastic deformation inside the

327 waterproofing membrane. Most FVMs are found in a central corridor inside the waterproofing
328 membrane (Fig. 8g) but also randomly distributed FVMs are present. Nevertheless, all FVMs
329 form between two heterogeneities present in the polymer matrix (Figs. 8f-h, 16a). This
330 implies that the incorporated particles govern (i) the spots at which microvoids and hence
331 also the craze-like microstructures initiate and (ii) their propagation pathway. Stress
332 concentration fields forming around the incorporated particles in polymer composites during
333 deformation are the reason for this dominance [66–68]. In theory, a polymer film containing a
334 single heterogeneity deforms in uniaxial tension. The position of the stress concentration
335 depends whether the heterogeneity is empty [13,63,64,68], mechanically softer [13,69,70] or
336 harder [13,63–65,69] than the matrix. Around pores and soft particle the stress concentration
337 will form at the equator of the particle [13,66,67] (Fig. 16b1). If the particle is harder, the
338 stress concentration will form around the pole of the particle [13,19,67] (Fig.16b2). The
339 investigated waterproofing membranes contain both, hard inclusions (quartz grains and
340 cement particles) and air pores. Hence, the FVMs should form at and run towards the
341 equators of air pores and form at and run towards the poles of any hard inclusion. Slight
342 mismatches occur between the theoretical positions and positions and propagation
343 directions in reality (Figs. 9, 16a). This is due to the fact that the individual stress
344 concentration fields around two heterogeneities which are in close vicinity interact
345 constructively and form a local stress concentration field at positions away from theoretical
346 positions [15]. As the plastic deformation (microvoids and FVM) form and propagate along
347 the maximum stress concentration deviations from ideal conditions occur (Fig. 9). Mapping
348 of the FVM propagation shows the influence of the respective heterogeneity. Quartz grains
349 cause a deviation towards their polar region (Fig. 5b orange rectangle, 9b, c black arrows)
350 along the grain-matrix interface. Around cement particles, microvoids form close to the polar
351 region. These observations indicate: (i) microvoids form at positions of maximum stress
352 concentrations, (ii) crazes propagate towards the spot of maximum stress concentration
353 around a rigid particle and (iii) the adhesion between quartz grains and polymer matrix is
354 weaker compared to the intrapolymer matrix strength. Contrarily, crazes propagate towards

355 the equator of an air pore (Figs. 5b blue rectangle, 9d,e white arrows) and terminate once
356 reaching the pore's interior (Fig. 9d, e). Here, (i) crazes propagate towards the maximum
357 stress concentration present around an air pore, (ii) the interfacial tension at the pore rim
358 between the polymer matrix and the air pore is weaker compared to the intra-polymer matrix
359 strength leading to a propagation of localized deformation into an air pore, where (iii) the
360 propagation stops because of dissipation of the deformational energy. This behaviour results
361 from the inverse relation between crack tip radius and crack energy [71–73]. Practical
362 applications of this behaviour is found, for example, by crack retardation in ceramics via
363 artificial incorporation of air pores, since there they decrease the crack tip energy by
364 increasing the crack tip radius [74]. A continuation of the FVM at the opposite pore rim is
365 possible as soon as the stress concentration at this point accumulates the energy needed for
366 the initiation and propagation of the FVM. The understanding of the FVM initiation and
367 propagation is also crucial to understand failure as cracking follows the FVM. Similar to
368 organic coatings [40], the initial crack in the waterproofing membrane starts at the substrate
369 membrane interface (Fig. 8f). With ongoing deformation several further cracks form and
370 grow (Fig. 8g, h). As the individual cracks are not connected and their start and end points
371 do not match up, these cracks must form at individual initiation spots contemporaneously at
372 sites where the fibrils of the FVM are stretched to their maximum. Neither the pathways nor
373 the perimeter of the cracks are straight. The deviation from a straight pathway occurs due to
374 the bending of the FVM around quartz grains. As crack propagation follows established
375 FVMs and these FVMs bend around quartz grains, therefore the cracks also bend around
376 them. The perimeter of the cracks is not straight due to the incorporation of air pores in the
377 crack. The FVMs run straight in between air pores, blunt in them and continue. Hence, any
378 crack following this FVM blunts in an air pore, splits the air pore and continues its
379 propagation along the FVM. The splitting up incorporates the air pore in the crack causing a
380 trace in the crack's perimeter in form of a lobe (pink dashed ellipse in Fig. 9a).

381 **4.3 Macroscopic deformation evolution**

382 Strain whitening is the macroscopic visual expression of plastic deformation in polymer-
383 modified mortars [42,43] as well as thermoplasts [75]. Changes in the microstructure cause
384 the whitening in polymer films [62,76,77]. These changes are either changes in the crystal
385 structure [62] or the formation of voids [62,76,77]. One possible structural change is strain-
386 induced crystallinity in originally amorphous polymers [56,58–60]. When taking voids into
387 account, studies suggest that Mie scattering causes the whitening [76,77]. Hence, the voids
388 must be in a size range similar to the wavelength of visible light [76]. In the investigated
389 waterproofing membrane, strain-induced crystallinity is a suggested deformation
390 mechanism, based on the size of the individual fibrils and voids inside the FVMs (see 4.1),
391 whereas the existence of microvoids in a suitable size range is observed (Fig. 10g).
392 Therefore, the observed strain whitening represents latest the stage of microvoid formation.
393 Additionally, dog bone data show that with the occurrence of strain whitening spots the bulk
394 sample is already in plastic deformation (Fig. 14). On the surface of the waterproofing
395 membrane, the width of the strain whitening zone grows with increasing opening of the
396 substrate gap (Fig. 6a) representing the evolution of the plastic deformation. Along the
397 thickness of the waterproofing membrane, all microscopic deformation structures appear in a
398 trapezoidal zone. Fringe pattern analysis [78–80] and x-ray microscopy [81] of different
399 materials covering a substrate show that (i) plastic deformation only occurs inside this zone
400 and (ii) that the geometry of this deformation zone is strongly dominated by the gap opening
401 in the substrate these materials cover. Hence, the combination of the trapezoidal geometry
402 along the membrane's thickness and the evolution of the strain whitening width define the
403 volume of the waterproofing membrane in which deformational energy can be dissipated by
404 the formation of aforementioned microstructures. The crucial parameter of this volume is the
405 opening angle (α) of the trapeze at the substrate gap. The strain whitening width on the
406 membrane's surface provides a first order link to the evolution of this opening angle α (Fig.
407 17). The changes of α define the evolution of the deformation volume. Plotting α against the
408 opening of the substrate gap is possible from the *Continuous Strain Whitening (CSW)*
409 onwards because prior to the *CSW* the whitening spots appear dispersal on the membrane's

410 surface. The plot (Fig. 18) shows two domains: (a) a constant increase in α and (b) α being
411 continuous. Domain (a) correlates with (i) the gap openings during which the number of
412 strain whitening spots increases on the membrane's surface while their respective size stays
413 similar (Figs. 6b, 18) and (ii) the increase of number of FVMs, their propagation towards the
414 membrane's surface and the initiation and propagation of cracks establishing the trapezoidal
415 deformation zone (Fig. 18). The increase in α , in number of strain whitening spots and in
416 number of FVMs and their propagation suggest that the membrane deforms actively during
417 this period of the crack-bridging, i.e. the deformational energy is used for the evolution of
418 microstructures. Along with the domain (b) goes (i) the change of the behaviour of the strain
419 whitening spots on the membrane's surface being constant in number and increasing in their
420 respective width (Figs. 6c, 18) and (ii) the connection of cracks through the thickness of the
421 membrane and decrease of numbers of FVMs inside the deformation zone (Fig. 8h).
422 Furthermore, the growth rate of the strain whitening width matches with the tensile
423 deformation speed of the rig (dashed in in Fig. 19) which indicates that the whitening spots
424 are stretched by at the rate of the rig's pulling speed. All these observations indicate that no
425 deformation-induced microstructures form inside the membrane but existing microstructures
426 are stretched passively during this period of crack-bridging with simultaneous stress
427 relaxation inside the membrane around cracks. Studies on pure polymer films verify a
428 maximum craze density [38] which suggests that the change from active deformation to
429 passive stretching occurs as soon as the accumulation of localised strain, i.e. number of
430 FVMs inside the deformation volume reaches its maximum. From that moment onwards,
431 stretching of existing FVMs provides the only possibility to dissipate additional deformation
432 energy. The *First Failure* indicates the moment at which anywhere in the waterproofing
433 membrane fibril rupture is continuous throughout the membrane's thickness. As rupture
434 occurs when the maximum stretch of a fibril is reached, the *First Failure* must occur after the
435 change from active deformation to passive stretch (Figs. 6a, 18, 19). Also, as the *First*
436 *Failure* is a local feature, the rest of the membrane is still able to deform with passive
437 stretching until fibril rupture is continuous throughout the membrane's thickness along a line

438 of the length of the membrane's width inside the strain whitening zone, the *Final Failure*
439 occurs (Figs. 6, 18, 19).

440 **4.4 Three-dimensional evolution of (micro)structures and bulk mechanics**

441 Imaging an infinite number of either thin sections lined-up behind each other or surfaces
442 stacked on top of each other, shows that the deformation evolution with all its related
443 structures is three-dimensional (Fig. 20). During the ongoing displacement, the
444 waterproofing membrane shows several microstructures at different positions inside the
445 membrane's volume (Figs. 8, 9, 20a). Hence at a fixed displacement, several deformation
446 mechanisms and multiple mechanical stages of the material, known from dog bone tests
447 (Fig. 14) are active simultaneously (Fig. 20a). The active deformation occurs after the elastic
448 yield up to peak stress (Figs. 14, 20a). Passive deformation lasts from peak stress to the
449 occurrence of the first failure in the dog bones (Fig. 14) and represents only a short period
450 during the stress–strain history of the material (Fig. 20). Linking the evolution of the
451 deformation mechanisms and associated microstructures with the stress–displacement data
452 from the dog bone tests shows that the mechanical state decreases from the substrate-
453 membrane interface to the membrane's surface (Fig. 20a) and that peak stress coincides
454 with the crack initiation at the membrane–substrate interface. From peak stress onwards
455 failure migrates through the membrane. Slices at fixed displacements and therefore time (t_1
456 to t_3 in Fig. 20a) demonstrate the spatial distribution of deformation structures and
457 mechanism (Fig. 20c). The slices along specific displacements (t_1 - t_3 in Fig. 20c) do not only
458 confirm the decreasing microstructural maturity towards the membrane's surface but also
459 show the progradational behaviour of the respective deformation mechanisms and their
460 associated structures (Fig. 20c). Both, the passive deformation and the failure, do not
461 propagate as a straight surface but as a progradational front containing lobes (Fig. 20c).
462 These peaks and troughs indicate that deformation structures do not initiate and propagate
463 simultaneously at a specific displacement but at different displacements inside the
464 membrane. Most likely the ubiquitously present heterogeneities cause this difference in the

465 point of initiation. Furthermore, these heterogeneities can cause spots inside the membrane
466 which show more mature deformation structures and mechanisms than their surrounding
467 (crack tip in the middle of the membrane in Fig. 9). A connection between these spots and
468 deformation structures propagating to the membrane's surface may connect and cause
469 additional lobes.

470 **5. Conclusions**

471 The investigated waterproofing membranes deform in an elasto-plastic manner. During the
472 plastic deformation, microvoids form and evolve to craze-like fibril-void microstructures
473 (FVM) with ongoing deformation. These FVMs evolve in the active part of the plastic
474 deformation, which is macroscopically seen in the appearance of whitening spots. During the
475 passive part, the now existing spots become stretched, which is macroscopically detectable
476 by the growth in their width. Plotting the strain whitening width in a width-displacement
477 diagram allow a macroscopic detection of the active and passive part of the plastic
478 deformation. The active part coincides with the steep slope in the diagram, while the
479 moderate slope represents the passive part.

480 Fibrils inside the FVMs rupture as soon as their maximum capability in stretching is reached.
481 This induces crack initiation and propagation. Cracking via fibril rupture initiates at the
482 substrate-membrane interface at peak stress of the crack-bridging test. Crack propagation
483 follows existing FVMs and a first continuous crack from interface to surface is observed
484 shortly after the change from active to passive deformation. From this moment onwards, the
485 membrane does not provide water tightness anymore and water might infiltrate into the
486 substrate potentially causing degradation. Based on these observations, the evolution and
487 growth of FVMs and subsequent fibril rupture indicates a ductile-to-brittle deformation
488 behaviour.

489 Inside the waterproofing membrane, stress concentrations build up at the incorporated
490 heterogeneities such as quartz grains, cement particles and air pores. They cause initiation

491 of new FVMs and deviation of existing FVMs. The position of the stress concentration, and
492 therefore the spots where FVMS either initiate or deviate to, depends on the type of
493 heterogeneity. Particularly, air pores act as an active retarder in crack propagation by
494 blunting the crack tip when a crack hits an air pore.

495 On sample scale, the FVMs define a trapezoidal zone spanning from the substrate-
496 membrane interface to the surface. This trapeze is the cross-section of the volume in which
497 all deformation takes place. Based on the strain whitening width on the membrane's surface
498 and the substrate gap opening, the opening angle α can be calculated. This angle is the
499 crucial parameter that determines the volume in which plastic deformation accommodates.
500 The change from the active part of the plastic deformation to the passive part possibly
501 occurs when the maximum FVM density is reached within the trapezoidal deformation
502 volume.

503 Further research should focus on the influence of intrinsic and extrinsic parameters on the
504 crack bridging behaviour of waterproofing membranes. This includes but is not restricted to
505 polymers of different Young's modulus, variations in temperature and/or deformation rate of
506 the tensile rig. Additionally, the influence of changes regarding the heterogeneities requires
507 closer investigations. The number, size and arrangement of both rigid particles and air pores
508 may affect the number, the initiation and/or propagation of FVMs and therefore either
509 prolong the active deformation part and/or retard crack initiation and growth. Furthermore,
510 the number, size and arrangement of air pores may aid the crack-bridging ability by
511 influencing the crack retardation effect positively.

512

513 **6. Acknowledgement**

514 The authors gratefully express their gratitude to Giuseppe Storti and Stefano Caimi from
515 ETH Zurich; Josef Kaufmann and Frank Winnefeld from EMPA and Srdan Kisin, Livio
516 Hegglin, Dragana Paripovic and Alexander Zapf from Nouryon for fruitful discussions and

517 input. Erwin Bühler and Hans Wicki from Nouryon are thanked for their patient introduction in
518 sample preparation and sample testing procedures. Mr. Dettmar is thanked for the careful
519 and well exerted preparation of the thin sections. Innosuisse, formerly known as Commission
520 for Technology and Innovation (CTI), is gratefully thanked for the financial support of project
521 No. 18797.1 PFIW-IW.

522 **7. References**

- 523 [1] C.A. Issa, P. Debs, Experimental study of epoxy repairing of cracks in concrete,
524 *Constr. Build. Mater.* 21 (2007) 157–163. doi:10.1016/j.conbuildmat.2005.06.030.
- 525 [2] M. Delucchi, A. Barbucci, G. Cerisola, Crack-bridging ability and liquid water
526 permeability of protective coatings for concrete, *Prog. Org. Coatings*. 33 (1998) 76–
527 82. doi:10.1016/S0300-9440(98)00012-5.
- 528 [3] S. Chandra, Y. Ohama, *Polymers in concrete*, CRC Press, 1994.
- 529 [4] Y. Ohama, *Handbook of polymer-modified concrete and mortars properties and*
530 *process technology*, Noyes Publications, New Jersey, 1995.
- 531 [5] J.E. Isenburg, J.W. Vanderhoff, Hypothesis for reinforcement of portland cement by
532 polymer latexes, *J. Am. Ceram. Soc.* 57 (1974) 242–245. doi:10.1111/j.1151-
533 2916.1974.tb10878.x.
- 534 [6] V.R. Riley, I. Razl, Polymer additives for cement composites: a review, *Composites*. 5
535 (1974) 27–33. doi:10.1016/0010-4361(74)90016-0.
- 536 [7] D. Van Gemert, L. Czarnecki, M. Maultzsch, H. Schorn, A. Beeldens, P. Łukowski, E.
537 Knapen, Cement concrete and concrete-polymer composites: two merging worlds: a
538 report from 11th ICPIG Congress in Berlin, 2004, *Cem. Concr. Compos.* 27 (2005)
539 926–933. doi:10.1016/j.cemconcomp.2005.05.004.
- 540 [8] R.P. Bright, T.J. Mraz, J.C. Vassallo, The influence of various polymeric materials on

- 541 the physical properties of a cementitious patching compound, in: L.A. Kuhlmann, D.G.
542 Walters (Eds.), Polym. Hydraul. Mix., American Society for Testing and Materials,
543 1993: pp. 44–62.
- 544 [9] J. Schulze, O. Killermann, Long-term performance of redispersible powders in
545 mortars, Cem. Concr. Res. 31 (2001) 357–362. doi:10.1016/S0008-8846(00)00498-1.
- 546 [10] H. Lutz, Waterproofing with cementitious slurries, Master Build. 3rd quarter (2005).
- 547 [11] S.I. Schneider, D.R. Dewacker, J.G. Palmer, Redispersible polymer powders for
548 tough, flexible cement mortars, in: L.A. Kuhlmann, D.G. Walters (Eds.), Polym.
549 Hydraul. Mix., American Society for Testing and Materials, 1993: pp. 76–89.
- 550 [12] J. Colville, A.M. Amde, M. Miltenberger, Tensile bond strength of polymer modified
551 mortar, J. Mater. Civ. Eng. 11 (1999) 1–5.
- 552 [13] G.H. Michler, F.J. Baltá-Calleja, Nano- and micromechanics of polymers structure
553 modification and improvement of properties, Carl Hanser Verlag, 2012.
- 554 [14] Q. Fu, G. Wang, Polyethylene toughened by rigid inorganic particles, Polym. Eng. Sci.
555 32 (1992) 94-97. doi:10.1002/pen.790320204
- 556 [15] Y. Huang, A.J. Kinloch, Modelling of the toughening mechanisms in rubber-modified
557 epoxy polymers - part I finite element analysis studies, J. Mater. Sci. 27 (1992) 2763–
558 2769. doi:10.1007/BF00540703.
- 559 [16] G.-M. Kim, G.H. Michler, Micromechanical deformation processes in toughened and
560 particle filled semicrystalline polymers: part 2. model representation for
561 micromechanical deformation processes, Polymer (Guildf). 39 (1998) 5699–5703.
562 doi:10.1016/S0032-3861(98)00169-4.
- 563 [17] C.M. Chan, J. Wu, J.X. Li, Y.K. Cheung, Polypropylene/calcium carbonate
564 nanocomposites, Polymer (Guildf). 43 (2002) 2981–2992. doi:10.1016/S0032-

- 565 3861(02)00120-9.
- 566 [18] T.H. Hsieh, A.J. Kinloch, K. Masania, J. Sohn Lee, A.C. Taylor, S. Sprenger, The
567 toughness of epoxy polymers and fibre composites modified with rubber
568 microparticles and silica nanoparticles, *J. Mater. Sci.* 45 (2010) 1193–1210.
569 doi:10.1007/s10853-009-4064-9.
- 570 [19] G.-M. Kim, G.. Michler, Micromechanical deformation processes in toughened and
571 particle-filled semicrystalline polymers: part 1. characterization of deformation
572 processes in dependence on phase morphology, *Polymer (Guildf)*. 39 (1998) 5689–
573 5697. doi:10.1016/s0032-3861(98)00089-5.
- 574 [20] C.B. Bucknall, Applications of microscopy to the deformation and fracture of rubber-
575 toughened polymers, *J. Microsc.* 201 (2001) 221–229. doi:10.1046/j.1365-
576 2818.2001.00838.x.
- 577 [21] L.C. Tang, Y.J. Wan, K. Peng, Y.B. Pei, L. Bin Wu, L.M. Chen, L.J. Shu, J.X. Jiang,
578 G.Q. Lai, Fracture toughness and electrical conductivity of epoxy composites filled
579 with carbon nanotubes and spherical particles, *Compos. Part A Appl. Sci. Manuf.* 45
580 (2013) 95–101. doi:10.1016/j.compositesa.2012.09.012.
- 581 [22] Y. Huang, A.J. Kinloch, Modelling of the toughening mechanisms in rubber-modified
582 epoxy polymers - part II a quantitative description of the microstructure-fracture
583 property relationships, *J. Mater. Sci.* 27 (1992) 2763–2769. doi:10.1007/BF00540703.
- 584 [23] R.A. Pearson, A.F. Yee, Toughening mechanisms in elastomer-modified epoxies -
585 part 2 microscopy studies, *J. Mater. Sci.* 21 (1986) 2475–2488.
586 doi:10.1007/BF01114294.
- 587 [24] G.H. Michler, Micromechanics of polymers, *J. Macromol. Sci. Part B.* 38 (1999) 787–
588 802. doi:10.1080/00222349908248139.

- 589 [25] Z.J. Tao, S.D. Ping, Z. Mei, Z.P. Cheng, Microstructure deformation and fracture
590 mechanism of highly filled polymer composites under large tensile deformation, J.
591 Phys. Conf. Ser. 419 (2013). doi:10.1088/1742-6596/419/1/012014.
- 592 [26] E.J. Kramer, Microscopic and molecular fundamentals of crazing, in: H.H. Kausch
593 (Ed.), *Crazing Polym.*, Springer-Verlag Berlin Heidelberg, 1983: pp. 1–56.
594 doi:10.1295/kobunshi.42.389.
- 595 [27] J. Rottler, M.O. Robbins, Growth, microstructure, and failure of crazes in glassy
596 polymers, *Phys. Rev. E - Stat. Physics, Plasmas, Fluids, Relat. Interdiscip. Top.* 68
597 (2003) 18. doi:10.1103/PhysRevE.68.011801.
- 598 [28] P.A. O'Connell, G.B. McKenna, Yield and crazing in polymers, in: *Encycl. Polym. Sci.*
599 *Technol.*, John Wiley & Sons, Inc, 2004: pp. 627–681.
600 doi:10.1002/0471440264.pst463.
- 601 [29] A. Makke, M. Perez, J. Rottler, O. Lame, J.L. Barrat, Predictors of cavitation in glassy
602 polymers under tensile strain: a coarse-grained molecular dynamics investigation,
603 *Macromol. Theory Simulations.* 20 (2011) 826–836. doi:10.1002/mats.201100006.
- 604 [30] P.A. O'Connell, M.J. Bonner, R.A. Duckett, I.M. Ward, The relationship between Slow
605 crack-propagation and tensile creep-behavior in polyethylene, *Polymer (Guildf).* 36
606 (1995) 2355–2362. doi: 10.1016/0032-3861(95)97333-B.
- 607 [31] S.K. Bhattacharya, N. Brown, Micromechanisms of crack initiation in thin films and
608 thick sections of polyethylene, *J. Mater. Sci.* 19 (1984) 2519–2532.
609 doi:10.1007/BF00550806.
- 610 [32] R.P. Kambour, A review of crazing and fracture in thermoplastics, *J. Polym. Sci.*
611 *Macromol. Rev.* 7 (1973) 1–154. doi:10.1002/pol.1973.230070101.
- 612 [33] A. Pawlak, A. Galeski, Cavitation during tensile deformation of polypropylene,

- 613 Macromolecules. 41 (2008) 2839–2851. doi:10.1021/ma0715122.
- 614 [34] A. Pawlak, A. Galeski, A. Rozanski, Cavitation during deformation of semicrystalline
615 polymers, *Prog. Polym. Sci.* 39 (2014) 921-958, doi:
616 10.1016/j.progpolymsci.2013.10.007.
- 617 [35] A. Krairi, I. Doghri, A thermodynamically-based constitutive model for thermoplastic
618 polymers coupling viscoelasticity, viscoplasticity and ductile damage, *Int. J. Plast.* 60
619 (2014) 163–181. doi:10.1016/j.ijplas.2014.04.010.
- 620 [36] R.N. Haward, B.M. Murphy, E.F.T. White, Relationship between compressive yield
621 and tensile behavior in glassy thermoplastics, *J. Polym. Sci. Part A* 9 (1971) 801–814. doi:10.1002/pol.1971.160090503.
- 622
- 623 [37] I.M. Ward, S. J., Mechanical properties of solid polymers, John Wiley & Sons Ltd,
624 2013. doi:10.1016/0032-3861(72)90129-2.
- 625 [38] A.S. Argon, J.G. Hannoosh, Initiation of crazes in polystyrene, *Philos. Mag.* 36 (1977)
626 1195–1216. doi:10.1080/14786437708239789.
- 627 [39] E. Riande, R. Díaz-Calleja, M.G. Prolongo, R.M. Masegosa, S. C., Yield crazing and
628 fracture, in: *Polym. Viscoelasticity Stress Strain Pract.*, Marcel Dekker, Inc., 2000: pp.
629 583–652.
- 630 [40] M. Delucchi, A. Barbucci, T. Temtchenko, T. Poggio, G. Cerisola, Study of the crack-
631 bridging ability of organic coatings for concrete: analysis of the mechanical behaviour
632 of unsupported and supported films, *Prog. Org. Coatings.* 44 (2002) 261–269.
633 doi:10.1016/S0300-9440(02)00054-1.
- 634 [41] M. Delucchi, A. Barbucci, G. Cerisola, Crack-bridging ability of organic coatings for
635 concrete: Influence of the method of concrete cracking, thickness and nature of the
636 coating, *Prog. Org. Coatings.* 49 (2004) 336–341.

- 637 doi:10.1016/j.porgcoat.2003.09.016.
- 638 [42] A. Volkwein, R. Petri, R. Springenschmid, Oberflächenschutz von Beton mit flexiblen
639 Dichtungsschlämmen, *Betonw. + Fert.* 9 (1988) 72–78.
- 640 [43] H. Zhao, W. Li, Y.M. Zhang, Study on crack bridging ability of polymer-modified
641 cement based compounds for waterproofing material, *Adv. Mater. Res.* 1129 (2015)
642 217–221. doi:10.4028/www.scientific.net/AMR.1129.217.
- 643 [44] A. Dubey, P.B. Groza, United States Patent Patent No .: US 9,302,448 B2, 2016.
- 644 [45] M. Waldvogel, R. Zurbruggen, A. Berger, M. Herwegh, Evidences for strain localisation
645 on surfaces of waterproofing membranes - a link between structures and mechanics,
646 in: H.B. Fischer, A. Volke (Eds.), 20. Int. Baustofftagung, Tagungsbericht, Band 2,
647 F.A. Finger-Institut für Baustoffkunde, Weimar, 2018: pp. 17–24.
- 648 [46] M. Waldvogel, R. Zurbruggen, A. Berger, M. Herwegh, Combined methods to
649 investigate the crack-bridging ability of waterproofing membranes, in: M.M.R. Taha
650 (Ed.), *Int. Congr. Polym. Concr. (ICPIC 2018)*, Springer International Publishing,
651 2018: pp. 249–254. doi:10.1007/978-3-319-78175-4.
- 652 [47] European Committee for Standardization, FprEN 14891 Liquid-applied water
653 impermeable products for use beneath ceramic tiling bonded with adhesives -
654 requirements, test methods, evaluation of conformity, classification and designation,
655 2011.
- 656 [48] European Committee for Standardization, DIN EN ISO 527 1-3 Plastics -
657 determination of tensile properties, 1996.
- 658 [49] J. Schindelin, I. Arganda-Carreras, E. Frise, V. Kaynig, M. Longair, T. Pietzsch, S.
659 Preibisch, C. Rueden, S. Saalfeld, B. Schmid, J.Y. Tinevez, D.J. White, V.
660 Hartenstein, K. Eliceiri, P. Tomancak, A. Cardona, Fiji: an open-source platform for

- 661 biological-image analysis, *Nat. Methods.* 9 (2012) 676–682. doi:10.1038/nmeth.2019.
- 662 [50] T. Wagner, H. Lipinski, IJBlob : an imagej library for connected component analysis
663 and shape analysis, *J. Open Res. Softw.* 1 (2013) 6–8.
664 doi:http://dx.doi.org/10.5334.jors.ae
- 665 [51] E.J. Kramer, Microscopic and molecular fundamentals of crazing, in: H. Kausch (Ed.),
666 *Crazing Polym.*, Springer-Verlag Berlin Heidelberg, 1983: pp. 1–56.
667 doi:10.1295/kobunshi.42.389.
- 668 [52] A.J. Kinloch, R.J. Young, *Fracture behaviour of polymers*, Springer Netherlands,
669 1995. doi:10.1007/978-94-017-1594-2.
- 670 [53] R.N. Haward, B.M. Murphy, E.F.T. White, Relationship between compressive yield
671 and tensile behavior in glassy thermoplastics, *J. Polym. Sci. Part A-2 Polym. Phys.* 9
672 (1971) 801–814. doi:10.1002/pol.1971.160090503.
- 673 [54] L.L. Berger, E.J. Kramer, Chain disentanglement during high-temperature crazing of
674 polystyrene, *Macromolecules.* 20 (1987) 1980–1985. doi:10.1021/ma00174a049.
- 675 [55] R.A.C. Deblieck, D.J.M. Van Beek, K. Remerie, I.M. Ward, Failure mechanisms in
676 polyolefines: the role of crazing, shear yielding and the entanglement network,
677 *Polymer (Guildf).* 52 (2011) 2979–2990. doi:10.1016/j.polymer.2011.03.055.
- 678 [56] A.M. Donald, The effect of temperature on the deformation and fracture of
679 polystyrene, *J. Mater. Sci.* 20 (1985) 2630–2638.
- 680 [57] H.H. Kausch, R. Gensler, C. Grein, C.J.G. Plummer, P. Scaramuzzino, Physics
681 crazing in semicrystalline thermoplastics, *J. Macromol. Sci. , Part B Phys.* 38 (1999)
682 803–815.
- 683 [58] A.B. Thompson, Strain-induced crystallization in polyethylene terephthalate, *J. Polym.*
684 *Sci.* 34 (1959) 741–760. doi:10.1002/pol.1959.1203412749.

- 685 [59] J. Richeton, S. Ahzi, K.S. Vecchio, F.C. Jiang, A. Makradi, Modeling and validation of
686 the large deformation inelastic response of amorphous polymers over a wide range of
687 temperatures and strain rates, *Int. J. Solids Struct.* 44 (2007) 7938–7954.
688 doi:10.1016/j.ijsolstr.2007.05.018.
- 689 [60] S. Jabbari-Farouji, J. Rottler, O. Lame, A. Makke, M. Perez, J.L. Barrat, Plastic
690 deformation mechanisms of semicrystalline and amorphous polymers, *ACS Macro*
691 *Lett.* 4 (2015) 147–150. doi:10.1021/mz500754b.
- 692 [61] L.A. Felton, P.B. O'Donnell, J.W. McGinity, Mechanical properties of polymeric films
693 prepared from aqueous dispersions, in: L.A. Felton (Ed.), *Aqueous Polym. Coatings*
694 *Pharm. Dos. Forms*, CRC Press, 2017: p. 400.
- 695 [62] B.W. Cherry, T.S. Hin, Stress whitening in polyethylene, *Polymer (Guildf)*. 22 (1981)
696 1610–1612.
- 697 [63] T. Juska, I.R. Harrison, A criterion for craze formation, *Polym. Eng. Sci.* 22 (1982)
698 766–776. doi:10.1002/pen.760221207.
- 699 [64] R.J. Oxborough, P.B. Bowden, A general critical-strain criterion for crazing in
700 amorphous glassy polymers, *Philos. Mag.* 28 (1973) 547–559.
701 doi:10.1080/14786437308221002.
- 702 [65] T.T. Wang, M. Matsuo, T.K. Kwei, Criteria of craze initiation in glassy polymers, *J.*
703 *Appl. Phys.* 42 (1971) 4188–4196. doi:10.1063/1.1659752.
- 704 [66] E.G. Kirsch, Die Theorie der Elastizität und die Bedürfnisse der Festigkeitslehre,
705 *Zeitschrift Des Vereines Dtsch. Ingenieure.* 42 (1898) 797–802.
- 706 [67] G.P. Tandon, G.J. Weng, Stress distribution in and around spheroidal inclusions and
707 voids at finite concentration, *J. Appl. Mech.* 53 (1986) 511-518.
708 doi:10.1115/1.3171804.

- 709 [68] W.D. Pilkey, D.F. Pilkey, Peterson's stress concentration factors, John Wiley & Sons,
710 2008. doi:10.1002/97804702111106.ch3.
- 711 [69] M. Matsuo, T.T. Wang, T. Kwei, Crazeing of polystyrene containing two rubber balls: A
712 model for ABS plastics, *J. Polym. Sci. Part A-2 Polym. Phys.* 10 (1972) 1085–1095.
713 <http://onlinelibrary.wiley.com/doi/10.1002/pol.1972.160100610/abstract>.
- 714 [70] G. Michler, Kriterien für den Größeneinfluß der Kautschukteilchen in schlagzähen
715 kautschukmodifizierten Polymeren, *Plaste Und Kautschuk*. 35 (1988) 347–350.
- 716 [71] A.A. Griffith, The phenomena of rupture and flow in solids, *Philos. Trans. Ser. A*. 221
717 (1920) 163–198.
- 718 [72] H.M. Westergaard, Bearing pressures and cracks, *J. Appl. Mech.* 6 (1939) 49–53.
- 719 [73] G.R. Irwin, Analysis of stresses and strains near the end of a crack traversing a plate,
720 *J. Appl. Mech.* 24 (1957) 361–364.
- 721 [74] Z.Y. Deng, J. She, Y. Inagaki, J.F. Yang, T. Ohji, Y. Tanaka, Reinforcement by crack-
722 tip blunting in porous ceramics, *J. Eur. Ceram. Soc.* 24 (2004) 2055–2059.
723 doi:10.1016/S0955-2219(03)00365-0.
- 724 [75] P. Wang, I.M. Hutchings, S.J. Duncan, L. Jenkins, E. Woo, Strain whitening of a
725 thermoplastic olefin material, *J. Mater. Sci.* 41 (2006) 4847–4859.
726 doi:10.1007/s10853-006-0066-z.
- 727 [76] Y. Lu, Y. Men, Cavitation-Induced Stress whitening in semi-crystalline polymers,
728 *Macromol. Mater. Eng.* 303 (2018) 1–31. doi:10.1002/mame.201800203.
- 729 [77] L. Farge, S. André, F. Meneau, J. Dillet, C. Cunat, A common multiscale feature of the
730 deformation mechanisms of a semicrystalline polymer, *Macromolecules*. 46 (2013)
731 9659–9668. doi:10.1021/ma4019747.
- 732 [78] P.M. Vitvitskii, V. V. Panasyuk, S.Y. Yarema, Plastic deformation around crack and

733 fracture criteria. A review, *Eng. Fract. Mech.* 7 (1975) 305–319. doi:10.1016/0013-
734 7944(75)90012-0.

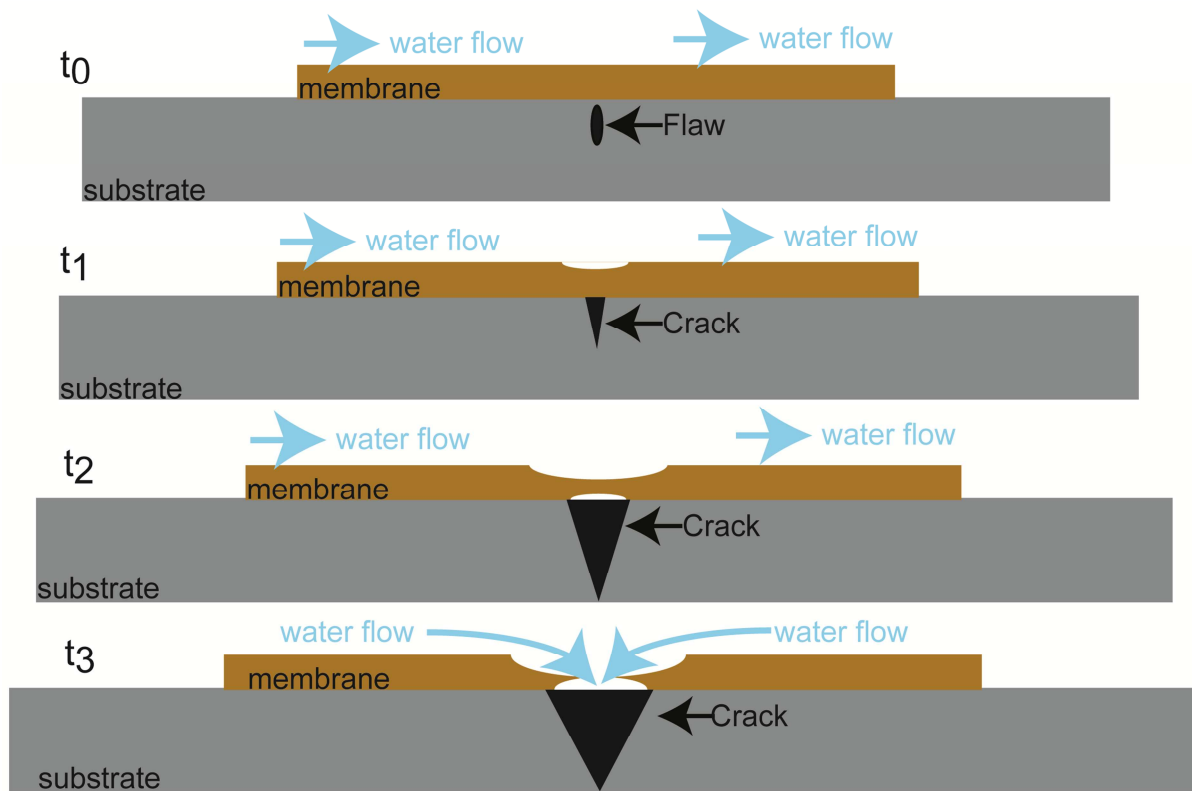
735 [79] K. Arakawa, K. Takahashi, Displacement fields around a crack tip in polymers, *Int. J.*
736 *Fract.* 86 (1997) 289–300. doi:10.1023/A:1007321906116.

737 [80] Y. Ju, H. Xie, X. Zhao, L. Mao, Z. Ren, J. Zheng, F.P. Chiang, Y. Wang, F. Gao,
738 Visualization method for stress-field evolution during rapid crack propagation using 3D
739 printing and photoelastic testing techniques, *Sci. Rep.* 8 (2018) 1–10.
740 doi:10.1038/s41598-018-22773-0.

741 [81] P.J. Withers, *A. Soc. Fracture mechanics by synchrotron X-ray microscopy*, *Philos.*
742 *Trans. R. Soc. A Math. Phys. Eng. Sci.* 373 (2015) 1–26.

743

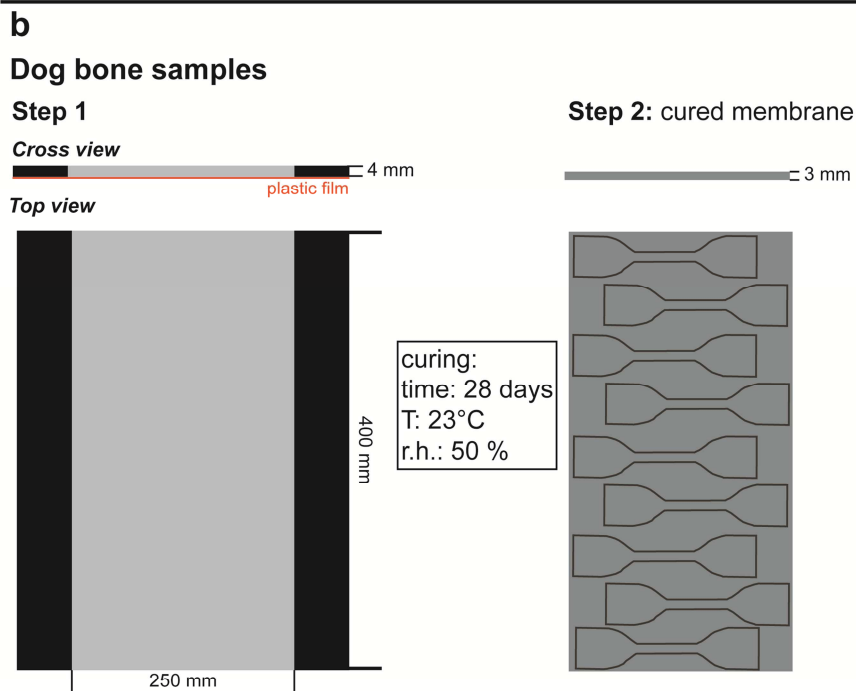
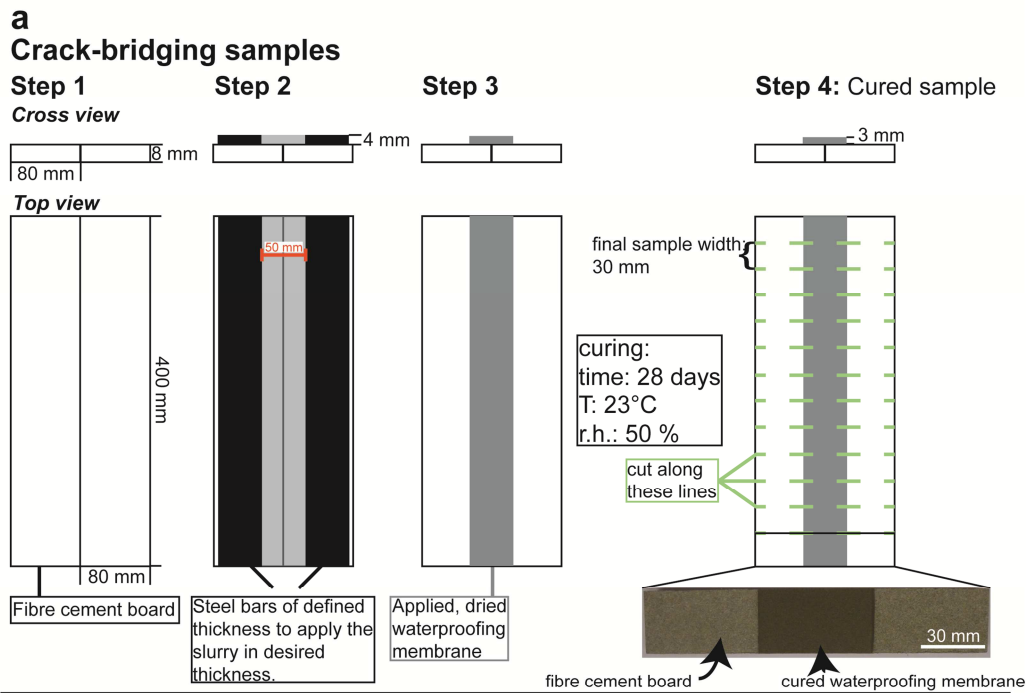
744



745

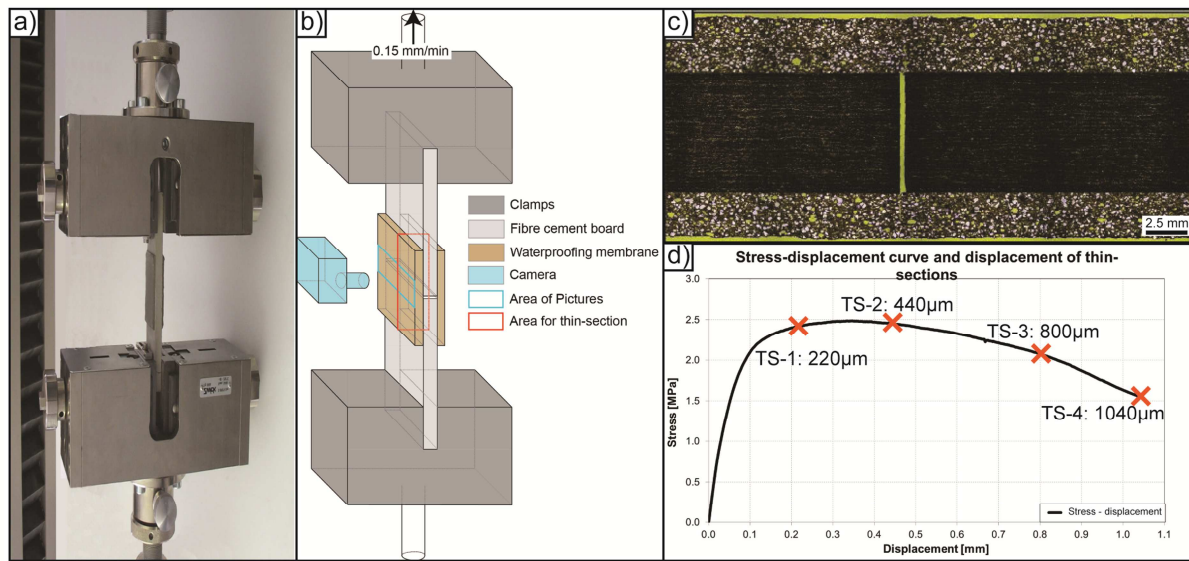
746 Fig.1: Sketch of the evolution of the crack-bridging ability (CBA) with time. At t₀, the
 747 membrane is in a relaxed state and a flaw is present in the substrate. With time, the flaw
 748 develops into a crack, the membrane becomes stretched and the CBA of the waterproofing
 749 membrane inhibits a cracking of the membrane (t₁ and t₂). At t₃, the CBA of the membrane
 750 is reached and the membrane ruptures. This allows water to infiltrate along a continuous
 751 crack and starts degradation of the substrate.

752



753

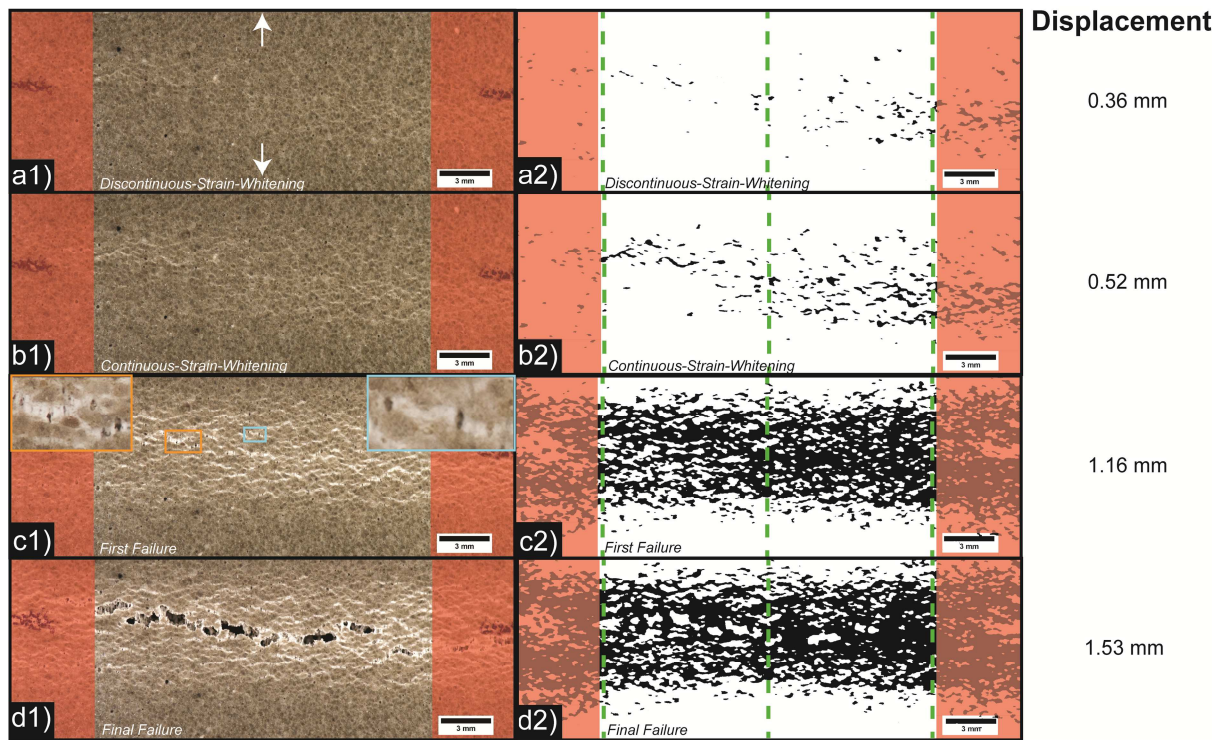
754 Fig. 2: Sample preparation: (a): Crack-bridging samples: Application of the freshly mixed
 755 slurry on the substrate (steps 1–3). The cured membrane is represented by a darker shade
 756 of grey. Step 4 shows the preparation of the samples for subsequent crack-bridging tests.
 757 (b): Dog bone samples: The fresh slurry is spread out and cured (step 1). Dog bone samples
 758 are punched out of the cured membrane (step 2).



760

761 Fig. 3: (a): Photograph of the universal tensile rig used for crack-bridging tests and dog bone
 762 tests with a crack-bridging sample placed in the machine. (b): Technical drawing of the
 763 crack-bridging test, the time-lapse photography as well as the geometry of later thin section
 764 plane. (c): Photograph of a thin-section of a sample being deformed up to a displacement of
 765 220 μm (TS-1 in d). Top and bottom layer represent waterproofing membranes which
 766 sandwich the two fibre board plates (dark grey). (d): Stress-displacement curve of a crack-
 767 bridging test showing the different displacement positions of the manufactured thin-sections.

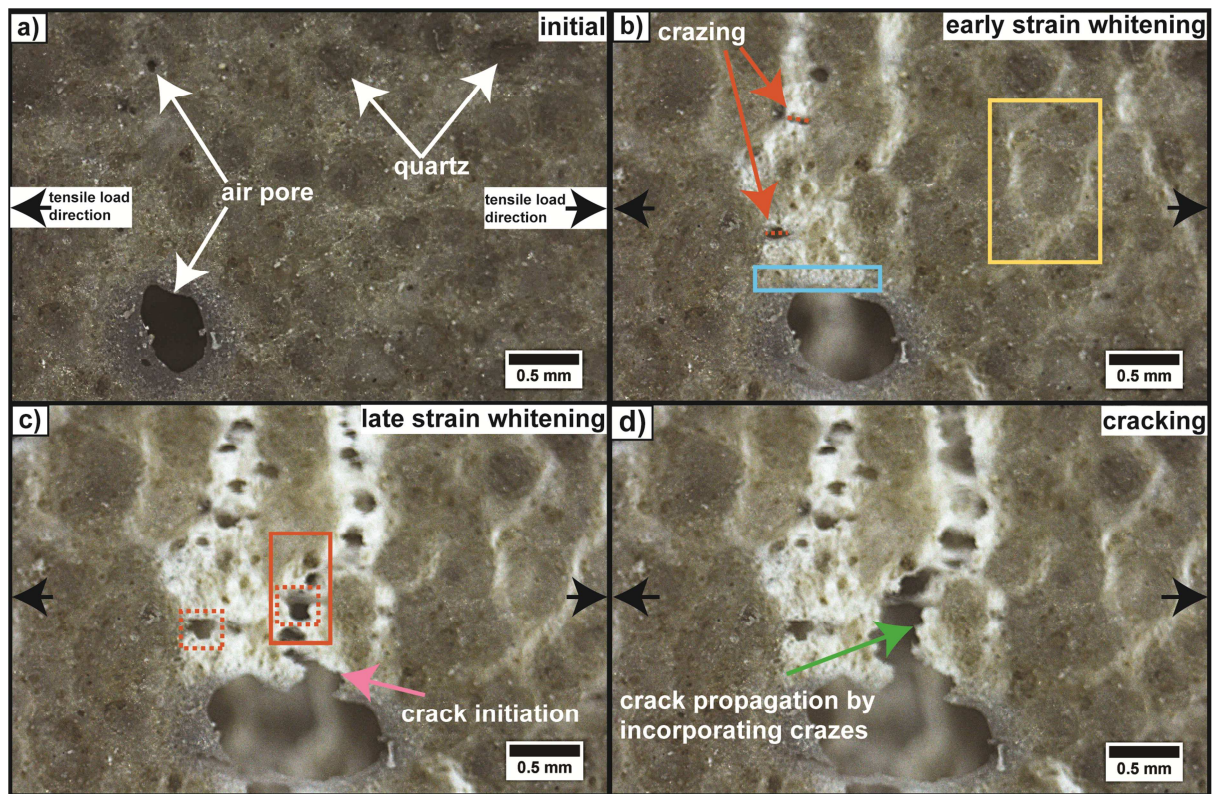
768



769

770 Fig. 4: (a1-d1) and (a2-d2) show the photos and segmented binary images, respectively, of
 771 the sample's surface as a function of progressive displacement for four main deformation
 772 stages: (a1) and (a2): Discontinuous-Strain-Whitening; (b1) and (b2): Continuous-Strain-
 773 Whitening; (c1) and (c2): First Failure (spots of loss of sealing capacity are magnified in the
 774 orange and blue rectangles in c1); (d1) and (d2): Final Failure. The white arrows in (a1)
 775 show the tensile load direction. The green dashed lines in (a2)-(d2) represent lines along
 776 which the number of the strain whitening spots and their widths were measured. The
 777 respective displacement of images (a1)-(d1) is noted on the right. See text for explanations.

778

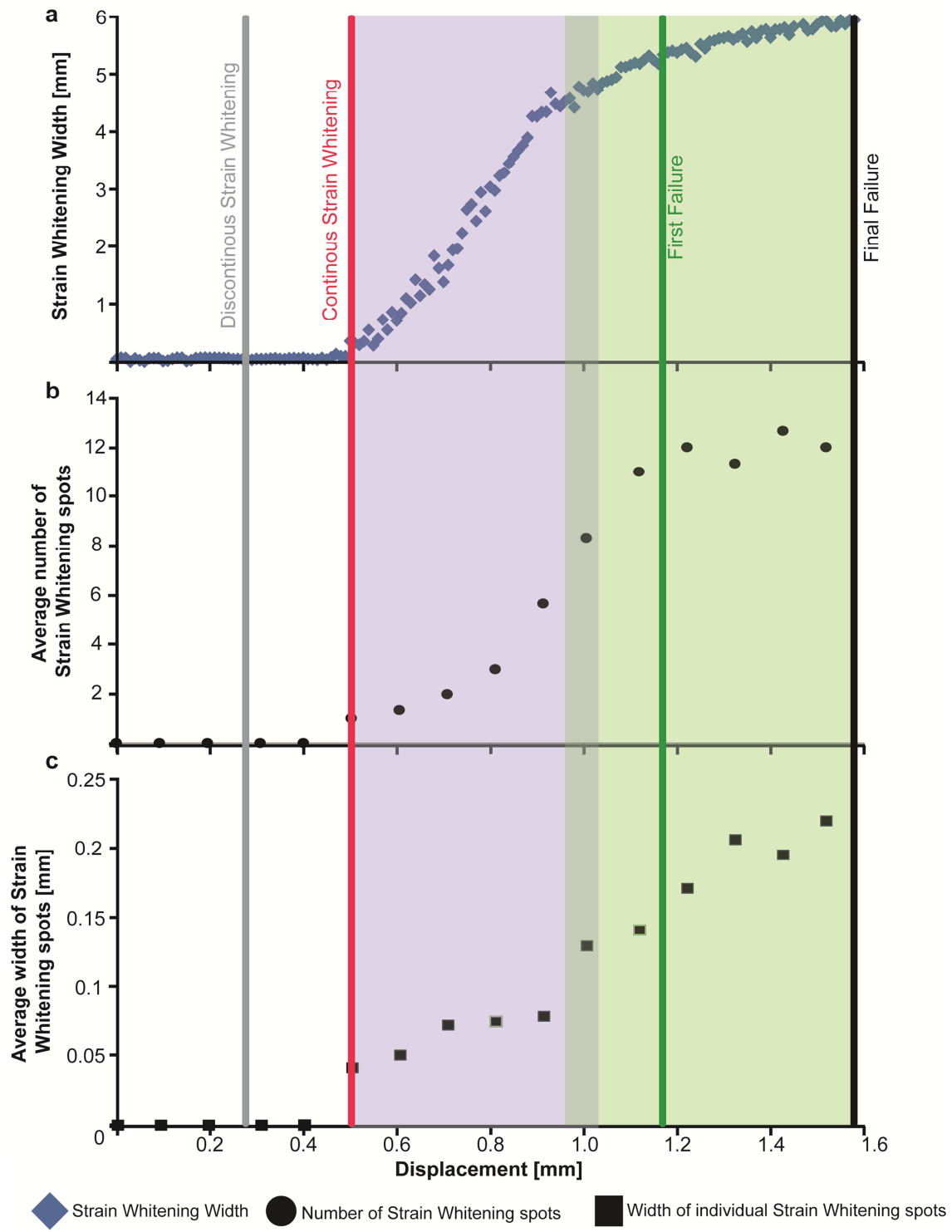


779

780 Fig. 5: Close-up photos of the surface of the waterproofing membrane for different
 781 deformation stages. (a): The surface of the waterproofing membrane shows quartz grains,
 782 air pores and the polymer-cement matrix. (b): Appearance of first elliptical holes with their
 783 long axes parallel to the tensile load direction (red arrows). Strain whitening lines bend
 784 around the quartz grains (orange rectangle) and run perpendicular to the pore rim (blue
 785 rectangle). (c): Several individual elliptical holes formed (red rectangle) and started to
 786 connect, i.e. form cracks. Cracking often nucleates at air pore rims (pink arrow). (d): Crack
 787 propagates into the cement-polymer matrix (green arrow). (For interpretation of the
 788 references to colour in this figure legend, the reader is referred to the Web version of this
 789 article.)

790

Strain Whitening Width, number and width of Strain Whitening spots

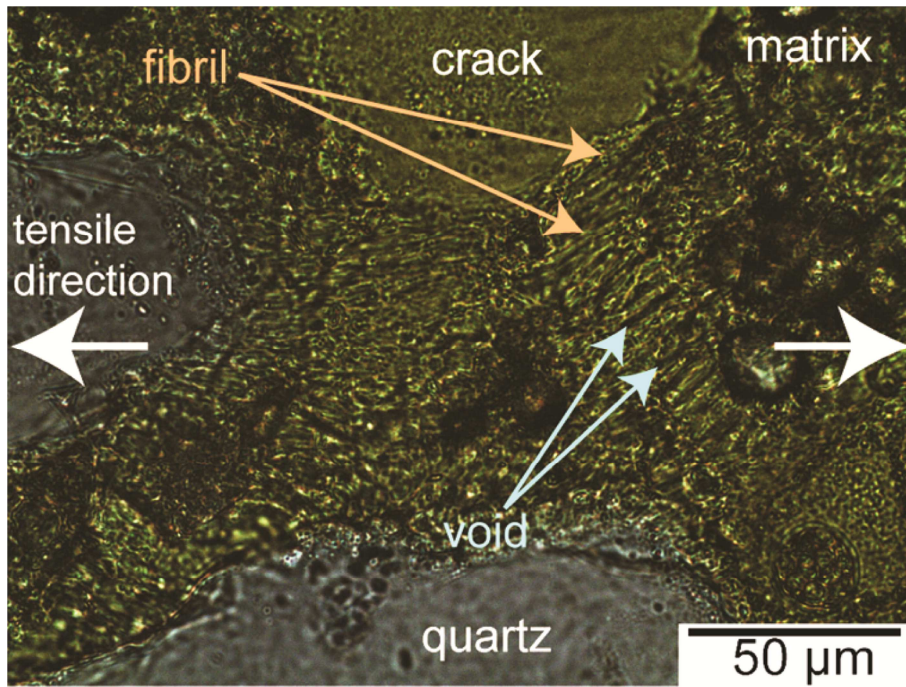


791

792 Fig.6: Diagrams show the evolution of microstructural features as a function of displacement.

793 The vertical lines represent important moments during the crack-bridging. (a): The evolution
794 of the Strain Whitening Width (SWW). (b): Average number of strain whitening spots along a

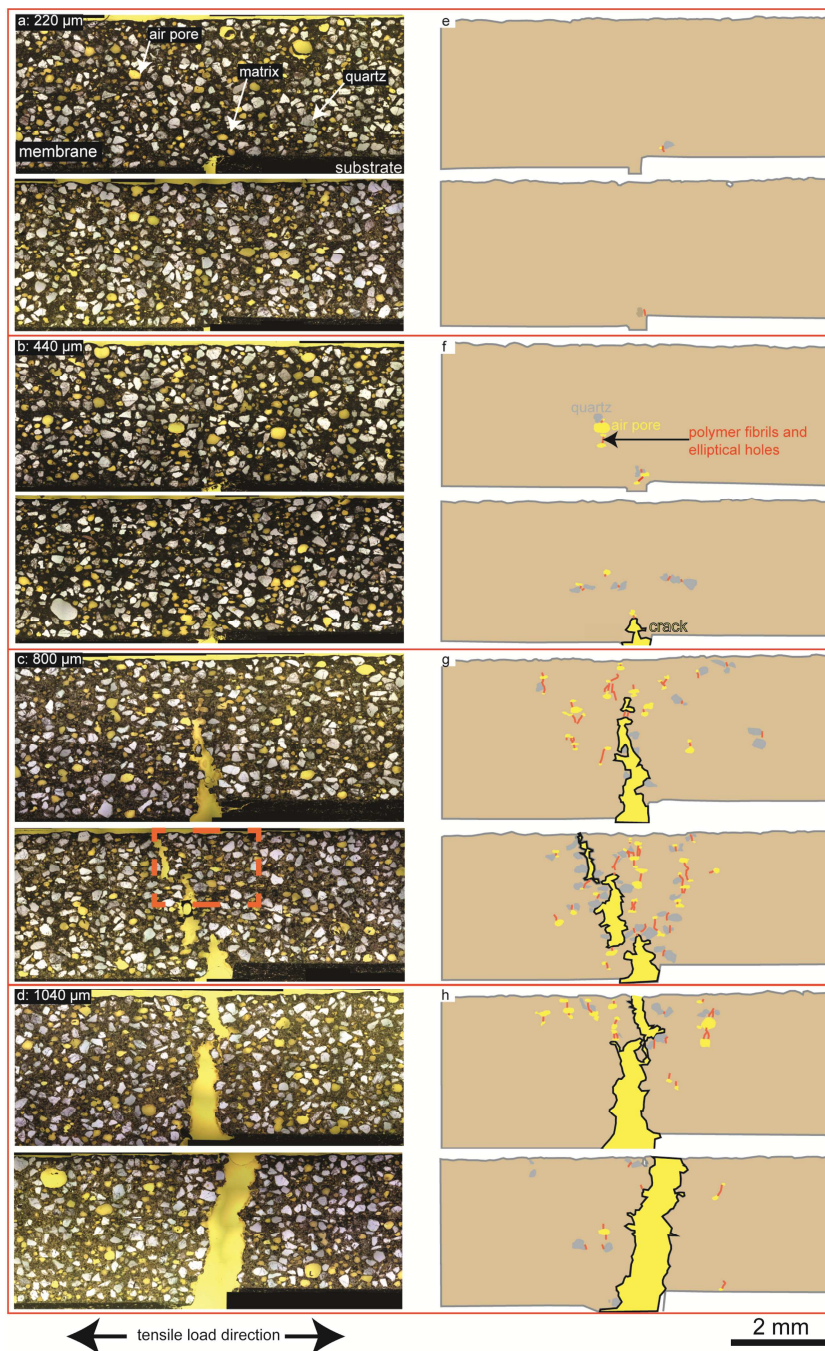
795 profile (Fig. 4) (c): Average width of the individual white spots along a profile (Fig. 4).



796

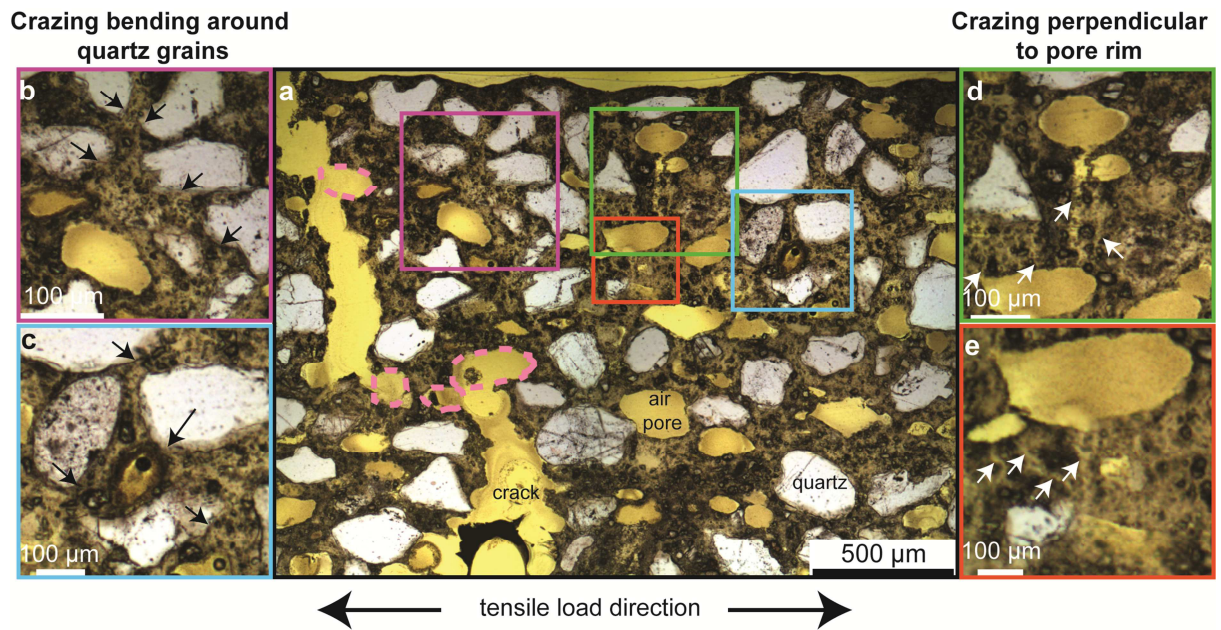
797 Fig. 7. Optical microscopy reveals the presence of deformed polymer film in the membrane
798 represented as stretched polymer fibrils (red arrows) and elliptical voids (blue arrows) in front
799 of a crack tip. The fibrils and voids are oriented subparallel to the tensile load direction. (For
800 interpretation of the references to colour in this figure legend, the reader is referred to the
801 Web version of this article.)

802



803

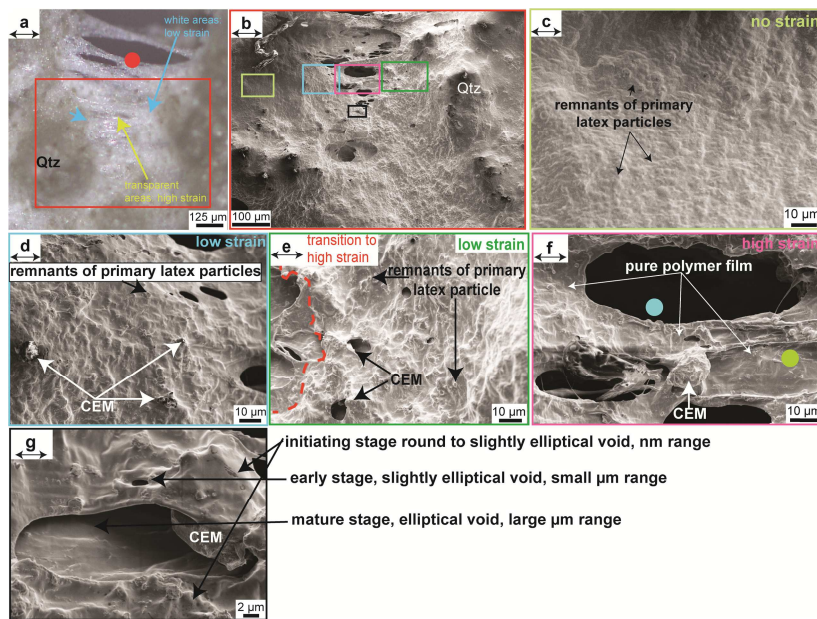
804 Fig. 8. (a)-(d): Photos of thin-sections (cut through the crack-bridging sample). At given
 805 displacement, every first and second image represent the upper and lower membrane,
 806 respectively, of the crack bridging sample (see Fig. 3c). (e)-(h): Corresponding maps show
 807 FVM deformation structures and associated heterogeneities in between which the FVMs
 808 initiate and propagate. The red dashed rectangle is a close up image in Fig. 9. Images were
 809 acquired from the entire thin-section. After the image acquisition, all images were cropped to
 810 show the membrane only and rotated with the substrate to bottom prior to mapping.



811

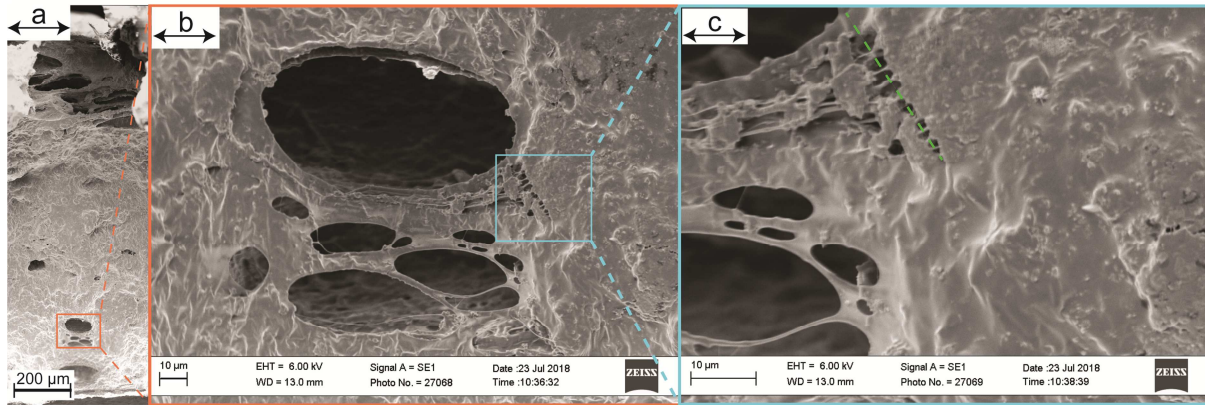
812 Fig. 9. (a): Close up view of a part of a thin-section (red dashed square in Fig. 8c) with
 813 probable former air pores (yellow) incorporated in the crack in pink dashed ellipses. (b) and
 814 (c): Crazing microstructures are deflected in close vicinity of quartz grains and follow the
 815 quartz-polymer matrix interface (black arrows). (d) and (e): Straight crazing trail in the
 816 polymer matrix perpendicularly oriented to the air pore boundary (white arrows).

817



818

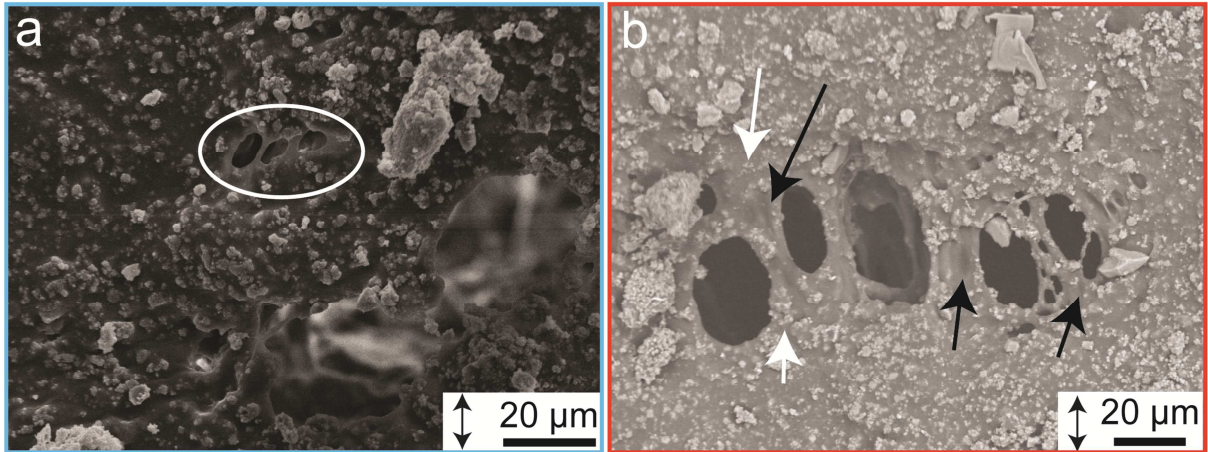
819 Fig. 10. Formation of fibril-void microstructures (surface view): The arrows, top left in all
 820 images, indicate the tensile load direction. All elliptical voids show an orientation of their long
 821 axis parallel to the tensile load direction. (a): Top view on a stretched waterproofing
 822 membrane under reflected light. Strained areas (arrows) bend around quartz grains. The red
 823 dot indicates the position of the profile along the thickness of the membrane in Fig. 11. (b)-
 824 (g) SEM investigation. (b): Overview of the area. The strained parts bend around quartz
 825 grains and cause a flat topography. (c): Non-strained polymer with topography caused by a
 826 quartz grain. Inside the polymer film many remnant structures of primary latex particles exist.
 827 (d): SEM view of a low strain part. Present cement grains cause minor topography found
 828 inside the polymer film. Small elliptical voids and few non-redispersed latex particles are
 829 found. (e): SEM view of a low strain area. The polymer film contains cement particles, small
 830 round to slightly elliptical voids and occasional non-redispersed latex particles. The red
 831 dashed line marks the transition to a high strain part. (f): SEM view of a high strain zone. The
 832 polymer film is strongly stretched, shows no topography and is free of cement particles. The
 833 flattened polymer film bends around cement particles. The voids are enlarged compared to
 834 (d) and (e). (g): Close up SEM view of a cement grain in strained polymer film. Voids initiate,
 835 grow and terminate at the cement grain. (For interpretation of the references to colour in this
 836 figure legend, the reader is referred to the Web version of this article.)



837

838 Fig. 11. (a): Cross view through the thickness of a waterproofing membrane: SEM profile
 839 along the red dot in Fig. 10a. The red dot in Fig. 10a corresponds to the top of the image.
 840 The tensile load direction is indicated by the black arrows. (b): An air pore in the polymer film
 841 with strained polymer film around. (c) The elliptical holes with strings of polymer film in
 842 between run from the rim of the pore into the matrix. Both features are oriented parallel to
 843 the tensile load direction.

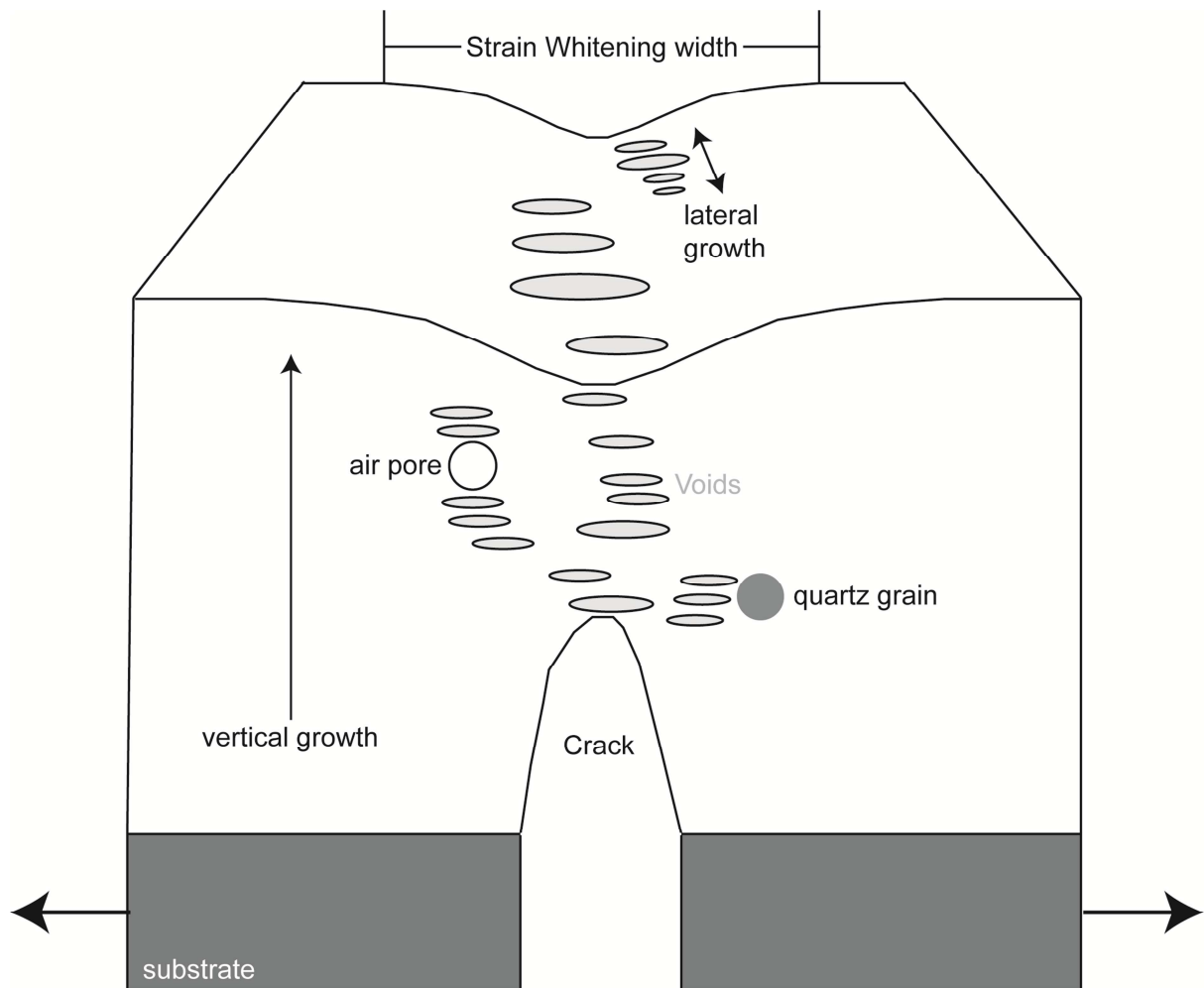
844



845

846 Fig. 12. Fibril-void microstructures: The double arrow in the bottom right of each picture
 847 indicates the tensile load direction. (a): Inside the white ellipse a FVM is present. A white rim
 848 forms around the fibrils and voids. Inside the white rim, no cement particles, which are
 849 ubiquitous in the unstrained membrane, are present. (b): In the centre of an FVM, the
 850 polymer fibrils are strongly strained and contain nearly no cement grains. Inside these fibrils,
 851 dark areas are found (black arrows). Less strained polymers containing cement particles
 852 surround this highly strained centre (white arrows). The entire FVM is encapsulated in non-
 853 strained polymer film, which contains several cement grains.

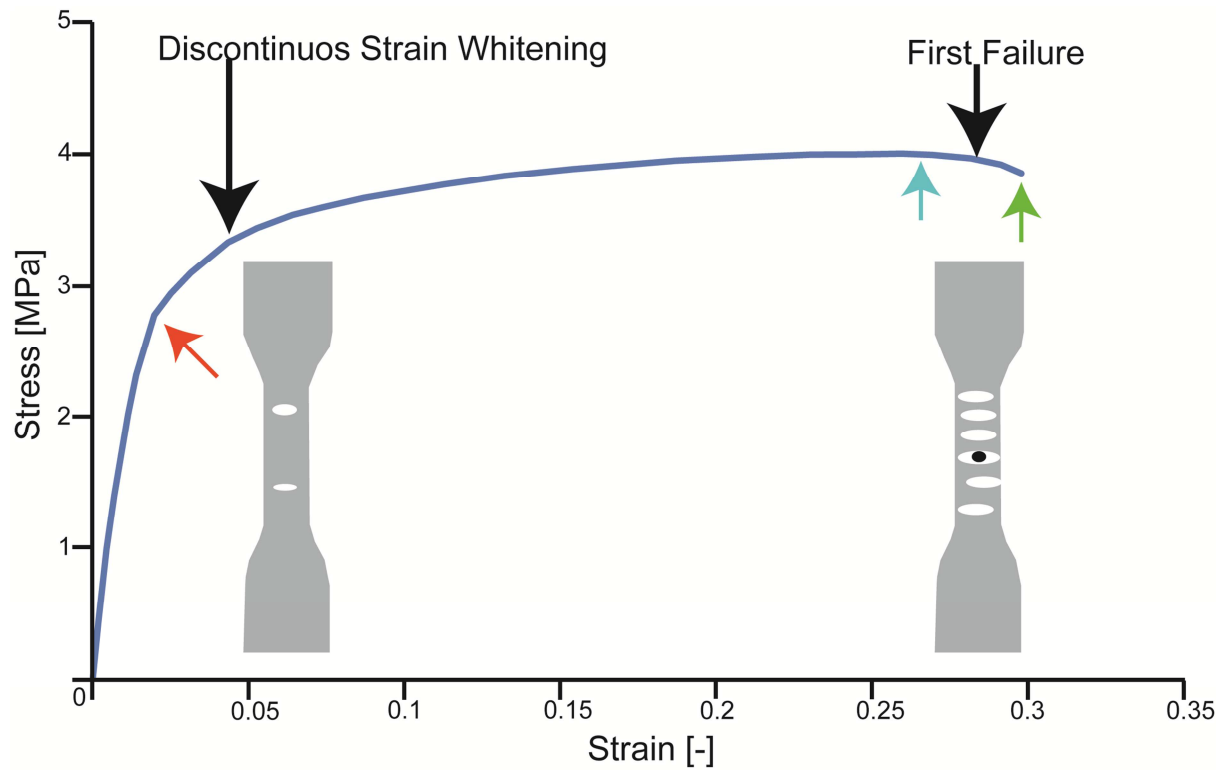
854



855

856 Fig. 13. Sketch of the 3D geometry of the fibril void microstructure (FVM): Sketched are only
 857 the voids. FVM initiates at cracks, hard inclusions (cement grains and quartz grains), and air
 858 pores. They can grow vertically through the membrane's thickness and laterally, e.g. on the
 859 membrane's surface. The type of inclusion governs the propagation orientation of the FVM.

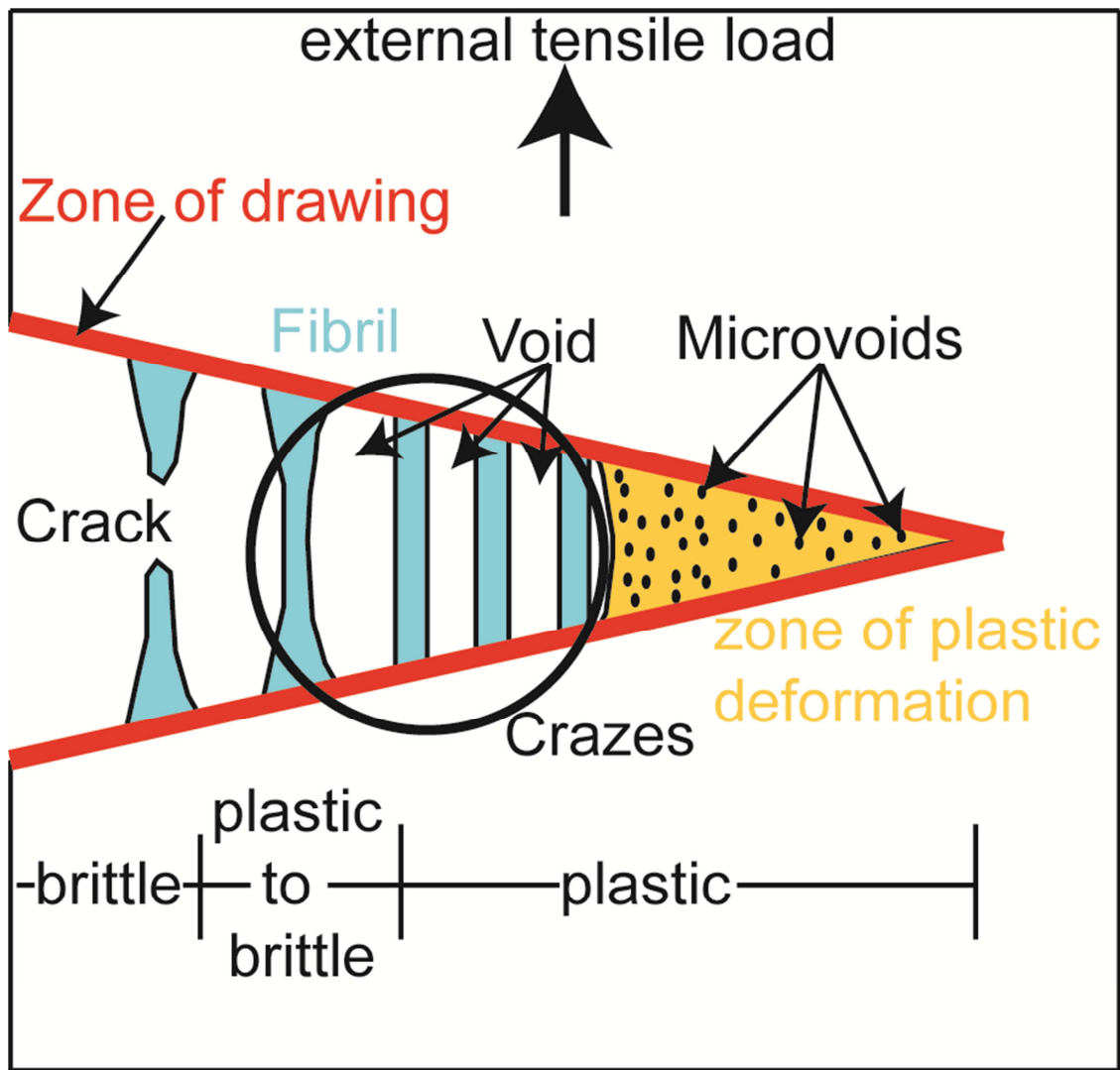
860



861

862 Fig. 14. Dog-bone tests of the waterproofing membrane: Stress-strain data from dog bones
 863 of the waterproofing membrane showing the elastic yield (red arrow), the peak stress (blue
 864 arrow) and the moment of failure of the entire dog bone (green arrow). The Discontinuous
 865 Strain Whitening on the surface of the dog bones appears after the elastic yield and is
 866 therefore a structure of permanent deformation. The First Failure (black spot) appears
 867 shortly after peak stress. (For interpretation of the references to colour in this figure legend,
 868 the reader is referred to the Web version of this article.)

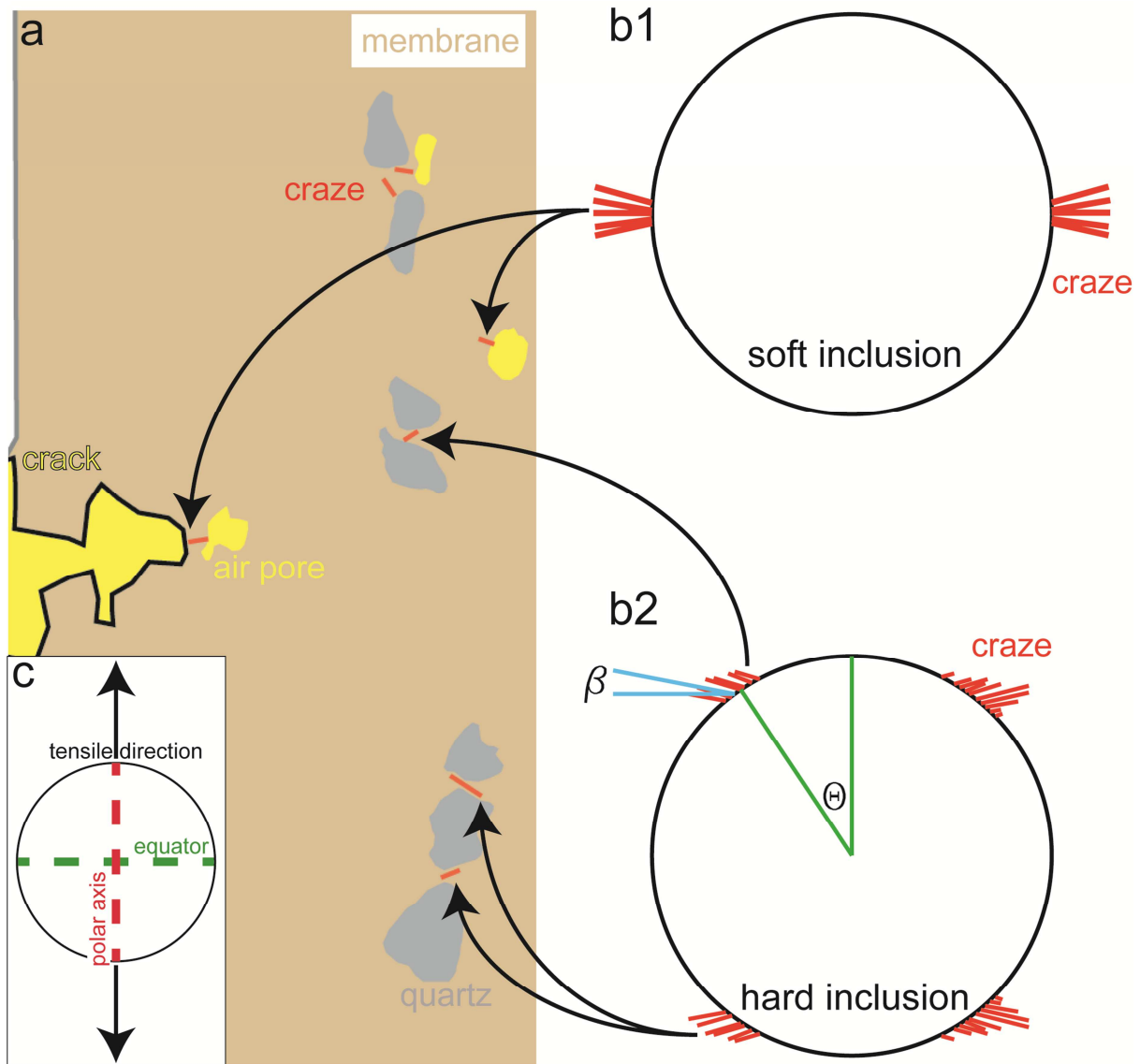
869



870

871 Fig. 15. Sketch of permanent deformation structures forming in pure polymer films. Crazes
 872 are expressed by fibrils and voids oriented parallel to the tensile load direction. Crack
 873 propagation is due to fibril rupture. Figure modified from Ref. [30].

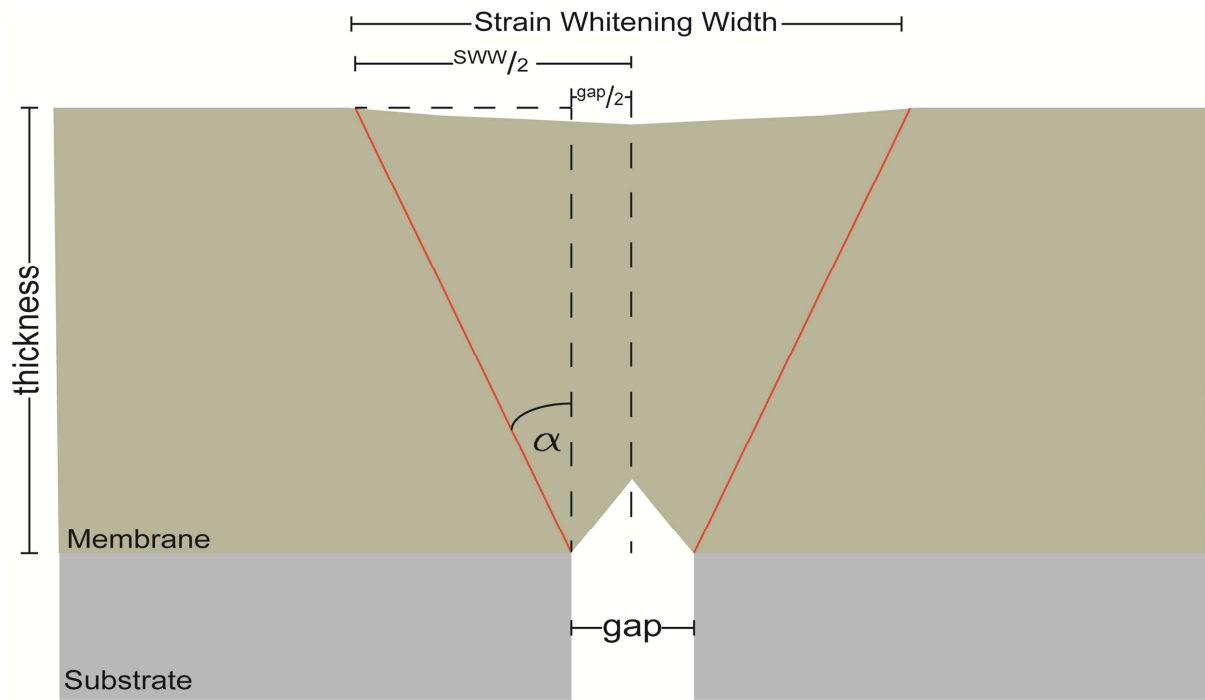
874



875

876 Fig. 16. Orientation of craze initiation positions as a function of the type of heterogeneity. (a):
 877 Mapping of air pores, quartz fillers and crazes at a displacement of 440 μm (Fig. 8f). (b1): In
 878 a soft inclusion in polystyrene crazes initiate at the equator and run (sub)perpendicular
 879 relative to the tensile load direction. (b2): In a rigid inclusion crazes initiate with an angle θ to
 880 the polar axis of the inclusion and run out with an angle β relative to the equator of the
 881 inclusion. Figures (b1) and (b2) are modified from Ref. [65]. (c): Sketch of orientation of the
 882 inclusion, its polar axis and equator with respect to the tensile load direction.

883

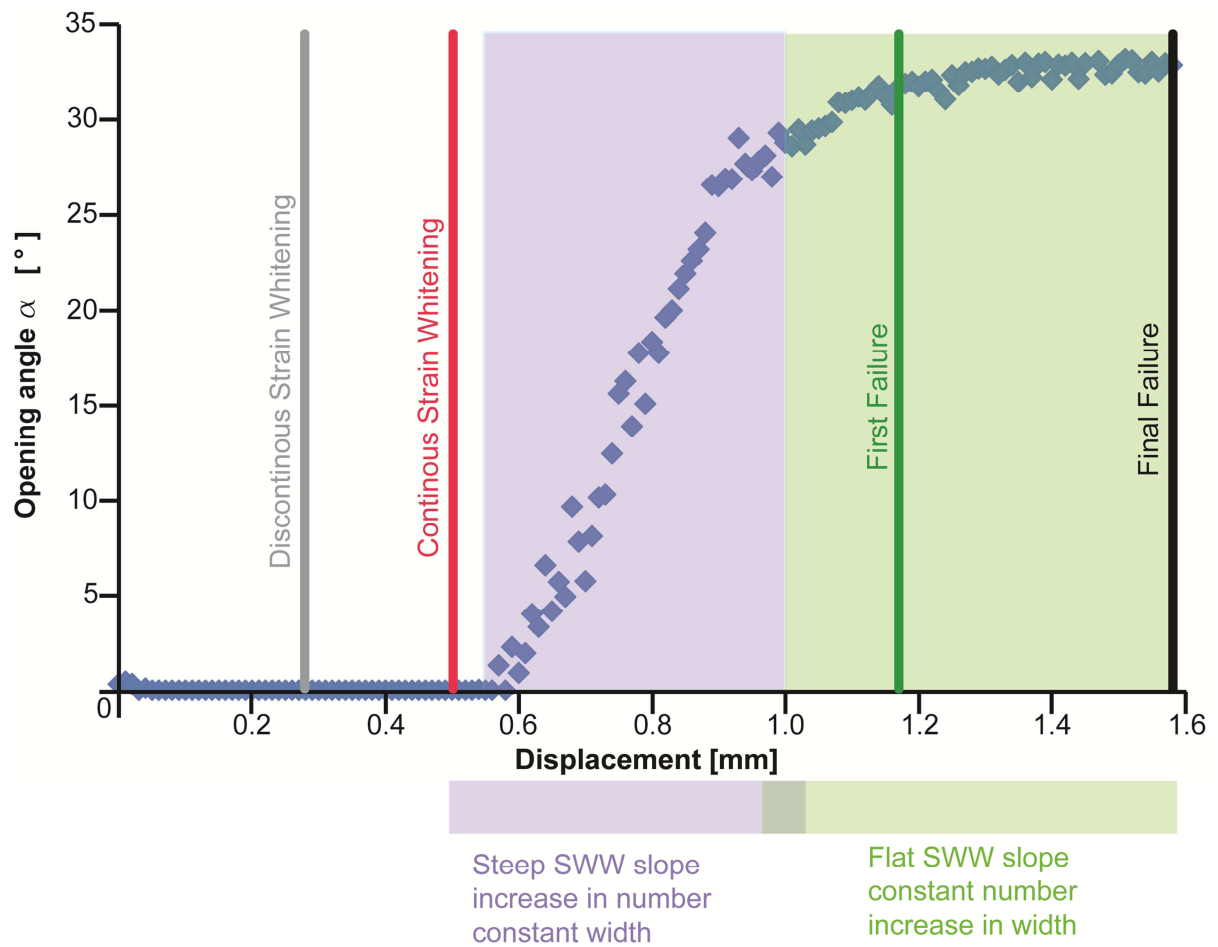


$$\tan(\alpha) = (SWW/2 - gap/2) / thickness = (SWW - gap) / (2 \times thickness)$$

884

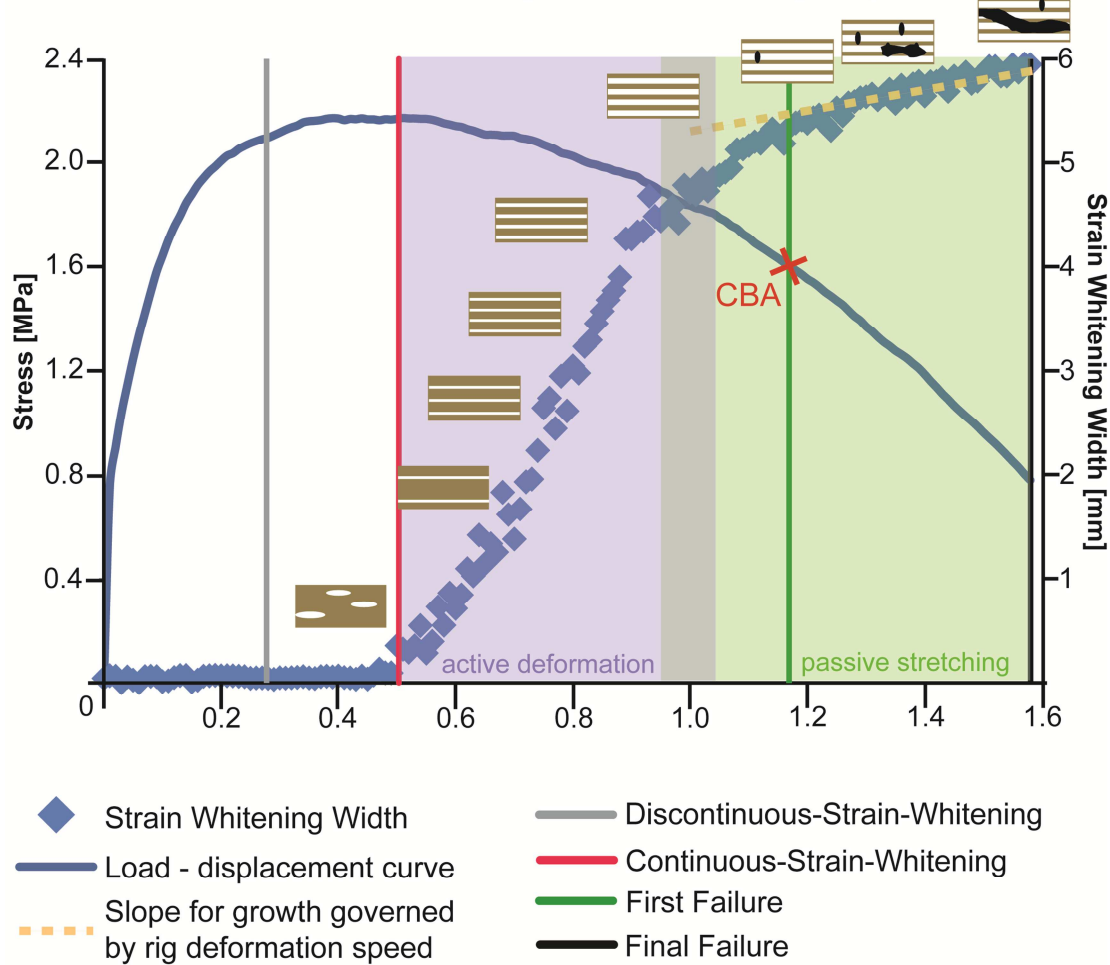
885 Fig. 17. Sketch of the relationship between the Strain Whitening Width (SWW) and the
 886 geometry of the zone in which deformation occurs. The activation angle α is the crucial
 887 parameter which defines the area of trapezoidal deformation zone.

888

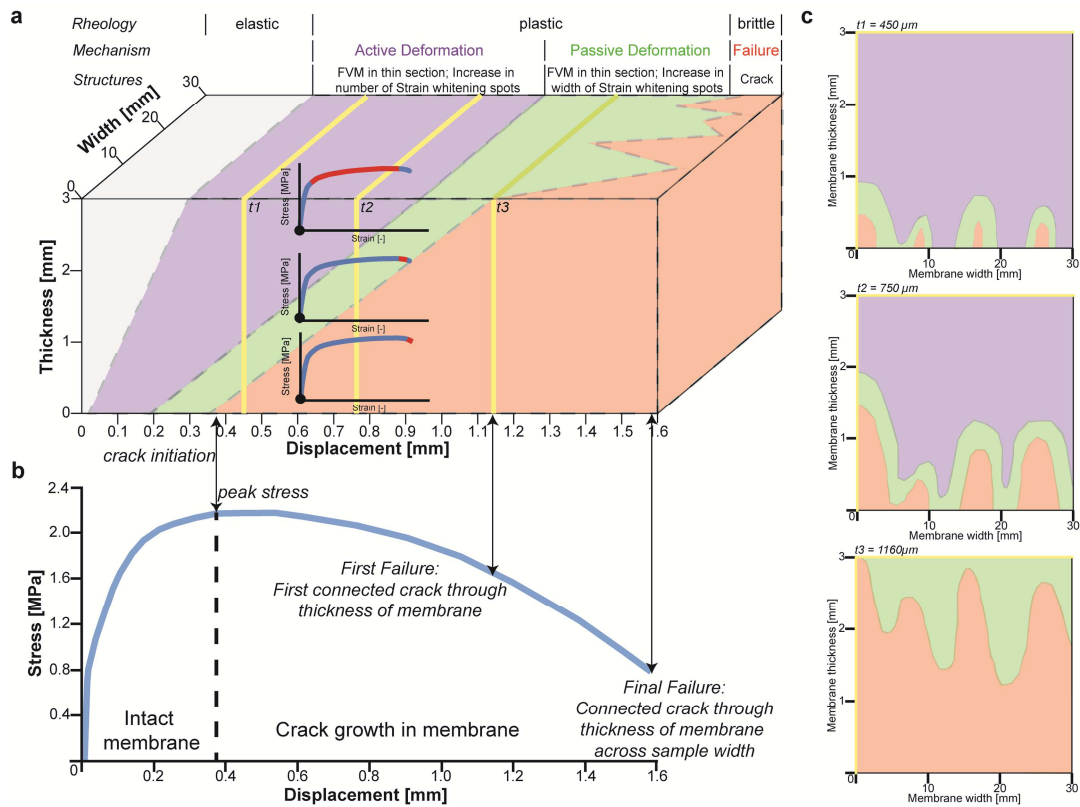


890 Fig. 18. Plot of the evolution of the opening angle α calculated from the SWW (Fig. 6a) with
 891 displacement. The opening angle starts to evolve with the Continuous Strain Whitening. The
 892 evolution of α shows a steep increase to ca. 33° at $950 \mu\text{m}$. This growth behaviour is
 893 followed by a constant value of α .

Stress and Strain Whitening evolution during displacement



896 Fig. 19. Connection between mechanical behaviour of the waterproofing membrane and
 897 deformation structures: The initiation of strain whitening spots on the membrane's surface
 898 coincides with the Discontinuous-Strain-Whitening and starts during plastic deformation of
 899 the membrane (see Fig. 14). During this stage, the crack-bridging sample is in a stress-
 900 increasing part. With the onset of the Continuous-Strain-Whitening (red line), the
 901 individual spots connect to white lines on the membrane's surface. Mechanically, the crack-
 902 bridging sample changes from the stress-increasing part to the stress decreasing part. The
 903 evolution of the Strain Whitening Width subdivides in an active accumulation (purple
 904 shaded), during which new white lines form, and a passive growth part (green shaded),
 905 during which existing white lines stretch. The match of the evolution of the Strain Whitening
 906 Width with the rig speed indicates that the rig speed is the dominant mechanism driving the
 907 passive stretching.



908

909 Fig. 20. Generalised sketch of the deformation evolution of waterproofing membranes during
 910 crack-bridging. (a): Evolution of (micro)structures (FVM) and deformation mechanisms inside
 911 the membrane's volume with increasing displacement and time during a crack-bridging test.
 912 During a specific displacement (e.g. 0.6 mm), the membrane shows several different
 913 mechanical stages (red parts of stress-strain curves from dog bone tests). Yellow lines
 914 represent slices through the membrane at fixed displacements and time (see c). (b): Stress–
 915 displacement diagram of corresponding crack-bridging test. The peak stress correlates to
 916 the crack initiation at the membrane-substrate interface. From peak stress onwards, cracks
 917 propagate from substrate-membrane interface to the surface. The First Failure (first
 918 connected crack through entire thickness of the membrane) does not influence the stress–
 919 displacement curve. (c): Slices through the membrane's volume at fixed displacements and
 920 time. The crack front forms lobes due to heterogeneities such as air voids and sand grains,
 921 which are not shown in this graphic. Their influence is shown in detail in Figs. 8 and 9. (For
 922 interpretation of the references to colour in this figure legend, the reader is referred to the
 923 web version of this article.)

924 Tab. 1: Weight percentage of the respective components in the waterproofing membrane.

Component	Quartz sand	OPC 52.5 N	RPP	Water
Wt.%	56	19	25	19

925

926 Tab. 2: Composition in weight fraction of the dry mix and volume fraction of the hardened
927 waterproofing membrane after all water is consumed and air is entrained during the mixing
928 process.

Component	Quartz sand	OPC 52.5 N	RPP	Air
Wt .%	56	19	25	-
Density kg/m³	2650	3100	938	-
Vol. %	37	11	40	12*

929

930 * Air pore content is based on point counting of air pores in thin sections

931

932 Tab. 3: Displacements of the prepared thin-sections and the position of sampling on the
933 stress-displacement curve (Fig. 3d).

Thin-section	Displacement [μm]	Position at stress-displacement curve
TS-1	220	After elastic part in stress increasing regime
TS-2	440	Shortly after peak stress, begin of stress decreasing
TS-3	800	Mature stress decreasing
TS-4	1040	First vertically continuous hole present

934